# STRUCTURE-ACTIVITY RELATIONSHIPS IN ACID-CATALYZED ALCOHOL DEHYDRATION REACTIONS

by

**Pavlo Kostetskyy**

Bachelor of Science in Chemical Engineering, Rowan University, 2010

Master of Science in Chemical Engineering, Rowan University, 2012

Submitted to the Graduate Faculty of

the Swanson School of Engineering in partial fulfillment

of the requirements for the degree of

Doctor of Philosophy

University of Pittsburgh

2018

UNIVERSITY OF PITTSBURGH

THE SWANSON SCHOOL OF ENGINEERING

This dissertation was presented

by

Pavlo Kostetskyy

It was defended on

April 12, 2018

and approved by

Karl J. Johnson, Ph.D., Professor, Department of Chemical and Petroleum Engineering

Peng Liu, Ph.D., Assistant Professor, Department of Chemistry

Götz Veser, Ph.D., Professor, Department of Chemical and Petroleum Engineering

Dissertation Director: Giannis Mpourmpakis, Ph.D., Assistant Professor, Department of Chemical and Petroleum Engineering

**STRUCTURE-ACTIVITY RELATIONSHIPS IN ACID-CATALYZED ALCOHOL DEHYDRATION REACTIONS**

Pavlo Kostetskyy, Ph.D.

University of Pittsburgh, 2018

The demand for primary energy sources and commodity chemicals has increased worldwide, as the global standards of living increase. The current reserves of petroleum have been declining, necessitating the use of alternative paths for energy generation and chemicals production. Biomass-derived fuels and chemicals offer an economically and environmentally attractive alternative to petroleum resources, diversifying our energy portfolio. Alcohols and polyols compose part of the biomass-derived product spectrum, which can be further converted to value-added chemicals. One important route is catalytic dehydration of alcohols – important reaction in biomass conversion with a high degree of industrial relevance.

We used electronic structure calculations to study acid-catalyzed alcohol dehydration in production of olefins and ethers – used in the synthesis of commodity chemicals and plastics. We focused on understanding dehydration reaction mechanisms, identifying rate-determining steps along reaction coordinates and identifying key physicochemical properties of catalysts that exhibit both Lewis- and Brønsted acidity, along with alcohols of varying size and substitution.

We have found that structure-activity relationships (SARs) can be developed by accounting for acid-base properties of catalysts and structure of reactants. Reaction barriers were

found to correlate with key physicochemical properties, used as reactivity descriptors towards development of predictive models. These properties can be used to inform the screening of a range of catalytic systems for the purpose of biomass upgrading via acid-catalyzed dehydration reactions.

In this work we report SARs developed for a series of catalysts and alcohols of varying size and substitution. The models exhibit flexibility in capturing fundamental system properties for a range of catalysts and reactant alcohols. Additionally, leveraging design principles based on structure-function observations, we designed first-of-their-kind, active and selective catalysts for the production of olefins from alcohols. SARs developed for alcohol dehydration on metal oxides were found to capture reactivity trends in alkane dehydrogenation over $Al_2O_3$, accounting for catalyst acid-base properties and stability of intermediates at key transition states.

## TABLE OF CONTENTS

## LIST OF TABLES

## LIST OF FIGURES

## PREFACE

I am very grateful to the many people who helped make this work possible. I would first like to thank my advisors and the members of my committee. Dr. Giannis Mpourmpakis guided my research and mentored me in number of aspects with tremendous clarity of vision, enthusiasm and patience throughout the duration of my time in his laboratory. Dr. Karl J. Johnson's advice was useful gaining a broader perspective of my work and its potential applications. Dr. Götz Veser provided valuable feedback on the experimental perspectives, limitations of computational work and how our findings could be implemented in a practical, laboratory setting. Dr. Peng Liu provided a unique perspective on approaching the systems examined in our work as a chemist.

I am grateful to our experimental collaborators for their valuable work, presented in tandem with our findings, namely Dr. Raymond J. Gorte at the University of Pennsylvania and Dr. Shik Chi Edman Tsang at the University of Oxford. I am also grateful to all of the undergraduate and graduate students who have helped make this work possible. I would like to thank the members of CANELA: Dr. Mudit Dixit, Ms. Natalie Austin, Mr. Michael Taylor, Mr. Zihao Yan, Mr. James Dean and Mr. Michael Cowan for their feedback, collaboration and assistance.

Finally, I would like to thank the members of my family, whose endless support, guidance and patience were a great help throughout my journey. My mother Lioubov, father Joseph, stepfather Michael, uncle Vasili and longtime friend/brother Jesse were indispensable in motivating and inspiring me toward accomplishing my goals.

# 1.0 INTRODUCTION

The rate of consumption of natural resource across the globe is increasing, exacerbated by large parts of the developing world achieving an improved quality of living standards, thus driving the rate of consumption[1-6]. Petroleum-derived fuels and chemicals are central to the global economy, used in countless applications ranging from food production to high-end electronics manufacturing. The production and consumption of these resources generates waste and results in emissions of greenhouse gases (GHG), largely responsible for the rapid changes to the climate of the Earth's biosphere. Alternative strategies for production of fuels and chemicals are needed to diversify our energy portfolio and create processes that are net carbon neutral in terms of atmospheric GHG emissions. Biomass is an abundant resource that can be processed into a range of products, offsetting the need for petroleum-based feedstocks and reducing the environmental impact of current production strategies.

## 1.1 BIOMASS-BASED PETROCHEMICAL ALTERNATIVES

Production of biomass-derived fuels and commodities as alternatives to petroleum-based products has been an active area of research in light of evidence of global climate change and increasing petrochemical resource prices[3-4, 6-9]. The depleting fossil fuel resources, increasing pollution and global warming concerns, require the utilization of alternative and sustainable

ways for the production of energy and chemicals[10]. Biomass is an abundant and inexpensive resource with a worldwide production of 560 billion tons of carbon[5]. Biomass-derived energy represents ~14% of the world's primary energy supply with 25% usage in developed and 75% in developing countries. The total sustainable worldwide biomass energy potential can correspond to as much as a third of the current global energy consumption[11]. Lignocellulosic biomass is the most promising renewable carbon energy source, as it is widely available around the world at a relatively low cost. It is composed of three main fractions: cellulose, hemicellulose, and lignin[12]. Although it is the most abundant plant material resource, its exploitation has been limited by its composite nature and rigid structure[13]. In view of these facts, the conversion of biomass feedstocks into valuable products has been investigated, usually in multistep processes using platform molecules of various structure and size as intermediates[14-15].

Glucose, fructose, polyols and simpler alcohols can be derived from cellulosic biomass processing and further converted into value-added chemicals. For instance, glucose can be reduced to sorbitol, which in turn, can be converted to simpler alkanes like hexane and used as a fuel, through a series of catalyzed dehydration and hydrogenation reactions[2]. Several processes currently exist to convert carbohydrates to liquid fuels. These include (among others) the formation of bio-oils by liquefaction or pyrolysis of biomass[16], the production of green gasoline, diesel and other biofuels via Fischer-Tropsch synthesis on biomass-derived syngas[17], and conversion of sugars and methanol to aromatic hydrocarbons over zeolite catalysts[18-19]. However, the conversion of glucose to ethanol through fermentation remains one of the most widely practiced processes[20]. The utilization of biomass derived alcohols (e.g. ethanol from biomass fermentation) instead of petroleum-based feedstocks can offset the petroleum load and reduce net $CO_2$ emissions.

The interest in alcohol dehydration reactions has increased in recent years because of its importance for producing higher-value chemicals and fuels from biomass derived compounds[1, 21-24]. As an example, dehydration of biomass derived alcohols can produce olefins, such as ethylene and propylene, which are important building blocks to produce polymers in the petrochemical industry. Dehydration chemistry also has the potential to be used to remove oxygen from more complicated molecules (e.g. glycerol to acrolein[25]), if selective pathways can be developed. In general, removal of oxygen from biomass increases energy density and the overall value of the products, making alcohol dehydration one of the most important reactions in the conversion of biomass to fuels and chemicals. Dehydration of biomass-derived alcohols via heterogeneous, acid-catalyzed alcohol dehydration at elevated temperatures is a plausible pathway to produce olefins, a critical feedstock in the formation of plastics, fibers, and other polymer products[26-28].

## 1.2 ACID-CATALYZED ALCOHOL DEHYDRATION: BASICS

Metal oxides are the traditional choice for alcohol dehydration catalysts[29-36]. However, even though this reaction has been a subject of research for more than half a century[29], our understanding of it is still limited. Surface hydroxylation that occurs via dissociative adsorption of water can significantly alter oxide catalytic properties and has been observed for a number of metal oxides. In the case of $\gamma$-$Al_2O_3$, Digne et al.[37-38] showed that different facets dehydrate at significantly different temperatures, with total dehydration occurring at ~600 K on the (100) surface but requiring temperatures in excess of 1000 K on (110) and (111) terminations.

Oxides of group IV metals (e.g. $ZrO_2$ [39-42] and $HfO_2$[43-44]) can also be hydroxylated and have demonstrated Lewis-acidity[45] (LA). In the case of $ZrO_2$, the dominant crystal facet has been shown to vary with sample preparation and the presence of impurities/dopants[41]. Piskorz et al. investigated a number of facets of t-$ZrO_2$, reporting dissociative adsorption of water in all cases, with molecular adsorption occurring only at high water coverage[41]. $ZrO_2$ also exhibits LA properties for reactions involving alcohols[46]. In evaluating its properties, Auroux et al. studied $ZrO_2$ for dehydration of 4-methyl-2-pentanol and identified surface composition as a key parameter in controlling selectivity of the desired alkene product[47].

Molecular adsorption of water was reported as energetically preferred on the (101) facet of anatase-$TiO_2$, while the (001) facet favors dissociative adsorption of water at low coverage[48]. Surface hydroxyl groups formed by dissociation of water on different phases of $TiO_2$ were also reported by several authors and shown to affect reaction rates and selectivities, with anatase shown to exhibit higher alcohol dehydration rates than rutile[49-51]. Of additional interest, it has recently been reported that $TiO_2$ exhibits Lewis acid sites that are catalytically active in water[45].

In addition to $Al_2O_3$, several oxides of group XIII metals have also shown activity in alcohol dehydration, namely gallium and indium ($Ga_2O_3$ and $In_2O_3$). Davis et al. have shown that gallium and aluminum oxides resemble each other closely in terms of catalytic activity and selectivity in the conversion of alcohols[34]. This similarity was further illustrated by Vimont et al.[52] who showed evidence of active LA sites as coordinatively-unsaturated gallium ions, and base sites as surface oxygen atoms. The similarity observed between alumina and gallia catalysts did not extend to indium oxide as demonstrated by Davis et al.[35]. $In_2O_3$ was shown to be an active catalyst for alcohol dehydration as well as dehydrogenation reactions by Umegaki et al.[53] Studies looking at surface properties of gallia and india have demonstrated that surface metal

acid sites can exist undercoordinated, as a result of oxygen vacancy formation on the catalyst surface[52, 54-57]. Lavalley et al. have studied γ- and α-$Ga_2O_3$ polymorphs and remarked on the similarity of surface composition and catalytic activity between $Al_2O_3$ and $Ga_2O_3$[57].

Alcohol dehydration catalyzed by γ-$Al_2O_3$ is known to produce ethers and olefins as major products with reaction selectivity shown to be a function of reaction conditions. Early experimental evidence for this reaction pathway was presented by Knözinger et al.[36] who performed dehydration experiments on γ-$Al_2O_3$ and found that the ether yield was a function of temperature and residence time. The authors suggested that ether formation occurred via a substitution reaction, favored at low temperatures[29, 36]. A scheme was proposed in which olefins can form through direct alcohol dehydration or through decomposition of ether to an olefin and an alcohol[29].

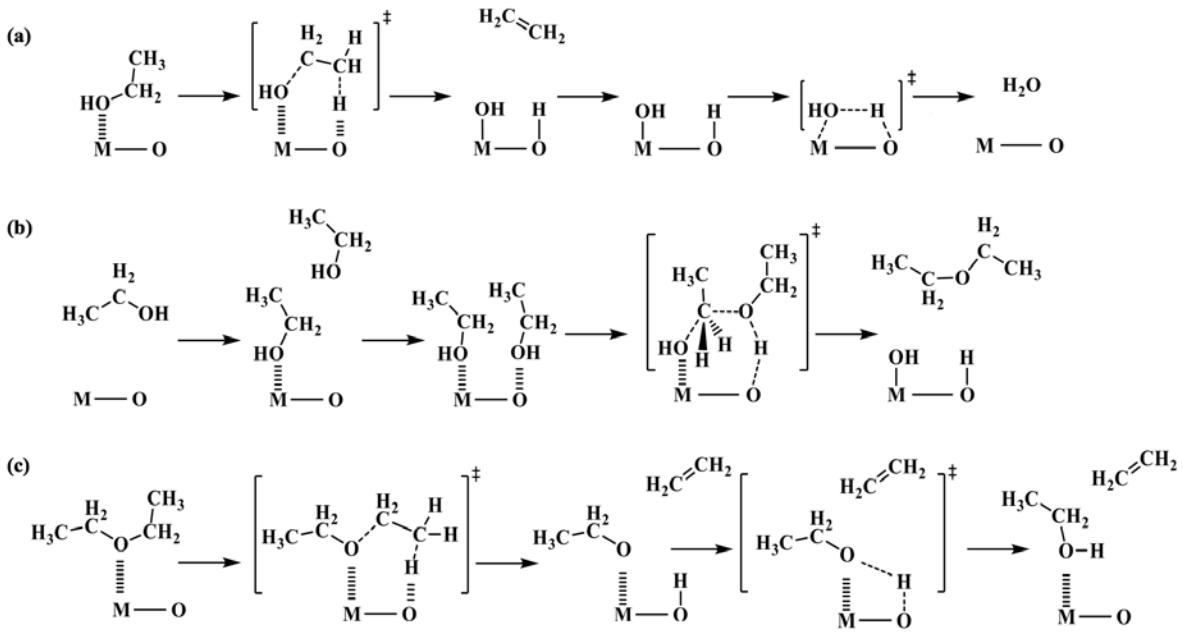

**Figure 1.** Alcohol dehydration mechanisms on γ-$Al_2O_3$ reported by Christiansen et al. (a) Unimolecular (E2) elimination mechanism of ethanol dehydration to ethylene on metal oxides, where M represents the metal Lewis acid site. (b) Bimolecular ($S_N2$) substitution mechanism on a metal oxide surface acid base pair. (c) Concerted ether decomposition mechanism.

Recent DFT work on alcohol dehydration on alumina has given unique insights into the dehydration reaction mechanisms [58-61]. It has been shown that olefin formation proceeds through a concerted elimination E2 type of mechanism, while ethers are formed via an $S_N2$ bimolecular substitution mechanism (Figure 1(a,b)). In addition, the authors proposed a secondary olefin formation route, in which ethers formed in the bimolecular substitution reaction catalytically decompose, forming an adsorbed alcohol and corresponding olefin (Figure 1 (a,b)). Christiansen et al.[58] showed that the diethyl ether decomposition energy barriers (over alumina) were within 1 kcal/mol of those of ethanol dehydration (ethylene production), suggesting competition between the two pathways.

Brønsted (e.g. zeolites) and Lewis (e.g. metal oxides) acid catalysts have been experimentally and theoretically shown to be active for alcohol dehydration. [27-29, 36, 58, 60, 62-66]. Metal oxides expose undercoordinated surface sites of acid-base (M-O) pairs that have been shown to catalyze dehydration reactions. However, though these alcohol dehydration reactions have been a subject of research for several decades[29], our understanding of the reactions on oxides remains limited. Specifically, a number of questions remain concerning surface reactivity in the presence of water, which is a product of the reaction. The dominant reaction mechanisms, nature of active sites and the effect of surrounding environment on the catalyst have not yet been answered and remain under debate in literature. DFT calculations can be used to study acid-catalyzed reactions and quantitatively compare the competing mechanisms on a model catalyst surface. DFT calculations allow for quantifying the physicochemical properties of the system (i.e. active site acidity/basicity and reactant stability), which may further be used to construct structure-activity relations (SARs) for relevant chemical reactions.

# 2.0 STRUCTURE-ACTIVITY RELATIONSHIPS ON METAL-OXIDES: ALCOHOL DEHYDRATION

The content of this chapter is taken in part from P. Kostestkyy, J. Yu, R. J. Gorte and G. Mpourmpakis, "Structure–activity relationships on metal-oxides: alcohol dehydration", *Catal. Sci. Technol.*, **2014**, 4, 3861-3869.[59]

## 2.1 COMPUTATIONAL METHODS

The dehydration mechanism of primary (ethanol, 1-propanol), secondary (2-propanol), and tertiary (2-methyl-2-propanol) alcohols was investigated on LA sites of $Ti_2O_2(OH)_4$, $Zr_2O_2(OH)_4$ and $Al_2O_2(OH)_2$ clusters by means of first principles theoretical calculations. These clusters represent catalytically active centers from partially hydroxylated oxide surfaces. In all these clusters, the ligands have been chosen so that the metal centers exhibit the oxidation states of the oxides (Ti, Zr: 4+, Al: 3+) and they are coordinated with both O and OH groups. We used the Becke's three-parameter hybrid (B3LYP)[67-68] and M06-2X[69] functionals with the 6-311G* triple-zeta basis set as implemented in Gaussian 09[70]. Similar cluster models and theoretical approach have been used in literature to simulate reactions on oxides[39, 71-74]. All reaction pathways were first mapped by scanning the potential energy surface of the reaction coordinate. The energy maximum that was found along the reaction coordinate was fully relaxed to a saddle point to

locate the actual transition state (TS). All transition states and local minima were obtained by full optimizations and verified by vibrational frequency and Intrinsic Reaction Coordinate (IRC) calculations.

## 2.2 RESULTS AND DISCUSSION

### 2.2.1 Role of Surface Hydroxylation in Dehydration Reactions

A number of unanswered questions remain debated in literature, regarding nature of the surface active sites and effect of water on catalyst activity at reaction conditions. Our preliminary studies have focused on using DFT calculations to investigate alcohol-dehydration mechanisms on metal oxides of $TiO_2$, $ZrO_2$ and $\gamma$-$Al_2O_3$. Specifically, we focused on the role of the different surface terminations (the presence of surface O or OH groups) in alcohol dehydrations. In Figure 2 we show the initial states of 1-propanol (stick) adsorbed on the three different clusters (ball and stick). All clusters consist of two bridge oxygen atoms connecting two metal centers and hydroxyl groups that terminate the clusters in a way that the metals maintain the oxidation states of the oxides. These clusters were constructed to represent the local chemical environment on the surface of these three oxides caused by dissociation of water, by incorporating OH functionalities.

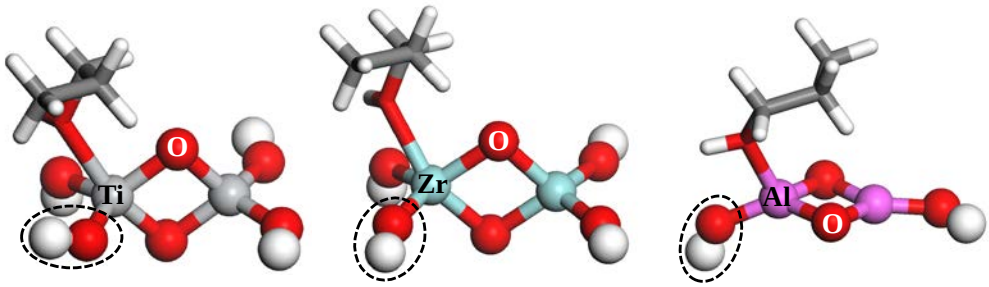


**Figure 2.** Cluster models of $TiO_2$, $ZrO_2$ and γ-$Al_2O_3$, involving both surface O (bridge O) and OH groups (dashed circle) with adsorbed 1-propanol on the metal center (Lewis acid site). The cluster is illustrated with ball and sticks representation, whereas the adsorbed alcohol with sticks.

The concerted E2 dehydration mechanism of the alcohols is energetically-preferred γ-$Al_2O_3$.[58, 60] According to this mechanism (Figure 1 (a)), a β-hydrogen of the alcohols is transferred to a surface oxygen of the oxide and the C-OH bond of the alcohol is depleted in a concerted reaction step. This mechanism involves a transition state with carbenium-ion characteristics. Under this mechanistic scheme, two centers on the metal oxides are responsible for the dehydration activity: the LA site (metal center) and its neighboring basic center (surface oxygen). The acidity of the metal and basicity of the surface oxygen atoms (acid-base pairs) are key physical properties controlling the performance of metal oxides as dehydration catalysts.

In Figure 3 we present the DFT-calculated barriers (B3LYP/6-311G*) of the E2 mechanism involving either the a) bridge O, or b) the OH groups of the oxide clusters shown in Figure 2, as a function of the carbenium ion stability (CIS) of the alcohols. CIS, defined in Equation (1), has been used as a descriptor of the type of the alcohol, as it was found that the alcohols exhibit carbenium ion (CI) characteristics in the transition state.

$$\text{CIS} = \left| E_{C_nH_{2n+1}}{}^{+} - E_{C_nH_{2n}} \right| \quad (1)$$

It can be noticed from Figure 3 that the dehydration barriers decrease as CIS increases. In addition, the barriers are consistently lower when involving the bridging O compared to those with the OH groups. The difference in energy barriers between the bridged O and the OH groups is small on $TiO_2$ and $ZrO_2$ but becomes pronounced in the case of γ-$Al_2O_3$. Another important observation is that the dehydration barriers on the cluster of γ-$Al_2O_3$ are smaller than on $TiO_2$ and $ZrO_2$, independent of whether or not bridged oxygens or OH groups are involved.

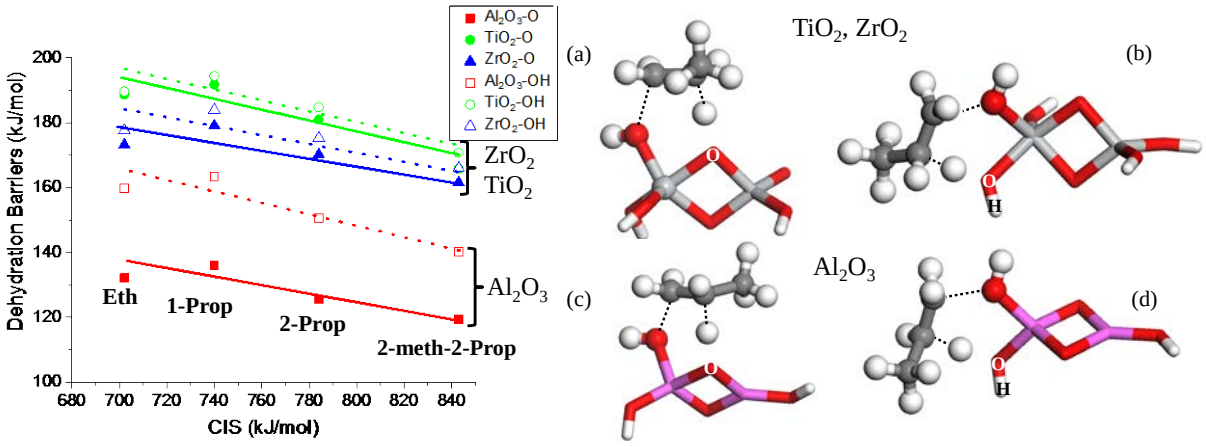


**Figure 3.** Calculated dehydration barriers (electronic energies) of Ethanol, 1-propanol, 2-propanol and 2-methyl-2-propanol on γ-$Al_2O_3$, $TiO_2$ and $ZrO_2$ involving surface O and OH groups (left figure) via a concerted E2 elimination mechanism (right figure) as a function of the CIS of the alcohols (absolute values). Lines are used as a guide to the eye (solid lines represent dehydration trends involving surface O and dashed, surface OH). All transition states on the clusters involving either O or OH groups for beta-H eliminations show CI characteristics, where the C-OH bond of the alcohol is significantly elongated compared to the beta C-H bond of the alcohol (transition states of 1-propanol dehydration involving surface O (a: $TiO_2$ and $ZrO_2$, c: $Al_2O_3$) and surface OH groups (b: $TiO_2$ and $ZrO_2$, d: $Al_2O_3$).

Proton affinity (PA) was used to quantify the basicity of O/OH sites and defined as the energy difference between protonated and neutral clusters (Equation (2), with the proton residing on the base site of the catalyst.

$$PA = E_{cluster+H^+} - E_{cluster} \quad (2)$$

It was shown that in all three oxides, the bridged O exhibits higher PA values than the OH groups, with the calculated PA values on the O and OH groups of the oxide clusters (in kJ/mol) as follows: O-$TiO_2$: -909.63, OH-$TiO_2$: -882.33, O-$ZrO_2$: -954.10, OH-$ZrO_2$: -897.75, O-$Al_2O_3$: -930.07, OH-$Al_2O_3$: -776.65. Summarizing the theoretical observations of Figure 3, γ-$Al_2O_3$ is a better dehydration catalyst than $TiO_2$ and $ZrO_2$ for alcohol dehydration reactions and $TiO_2$ and $ZrO_2$ show the same dehydration activity. The results of our calculations are presented in Figure 4, where we show the dehydration (free energy) barriers as a function of the CIS of the alcohols and the PA of the basic center. In this figure we also show the binding energy (BE), calculated using Equation (3), of the alcohols on the different oxides (absolute values). Similar to PA, binding energies were calculated by finding the difference in energies of alcohols bound on the Lewis acid site and individual (gas phase) cluster and alcohol energies.

$$BE = E_{ads} - E_{cluster} - E_{alcohol} \quad (3)$$

All alcohols bind the LA site with the same strength and there is no dependence on the type of alcohol. However, alcohols bind much stronger the Al acid site (BE=-133.0 kJ/mol) than the Ti and Zr (-70.8 and -83.1 respectively). This binding behavior correlates with the

dehydration trends on the different oxides: the stronger the BE of the alcohol, the lower the activation energies on the oxides.

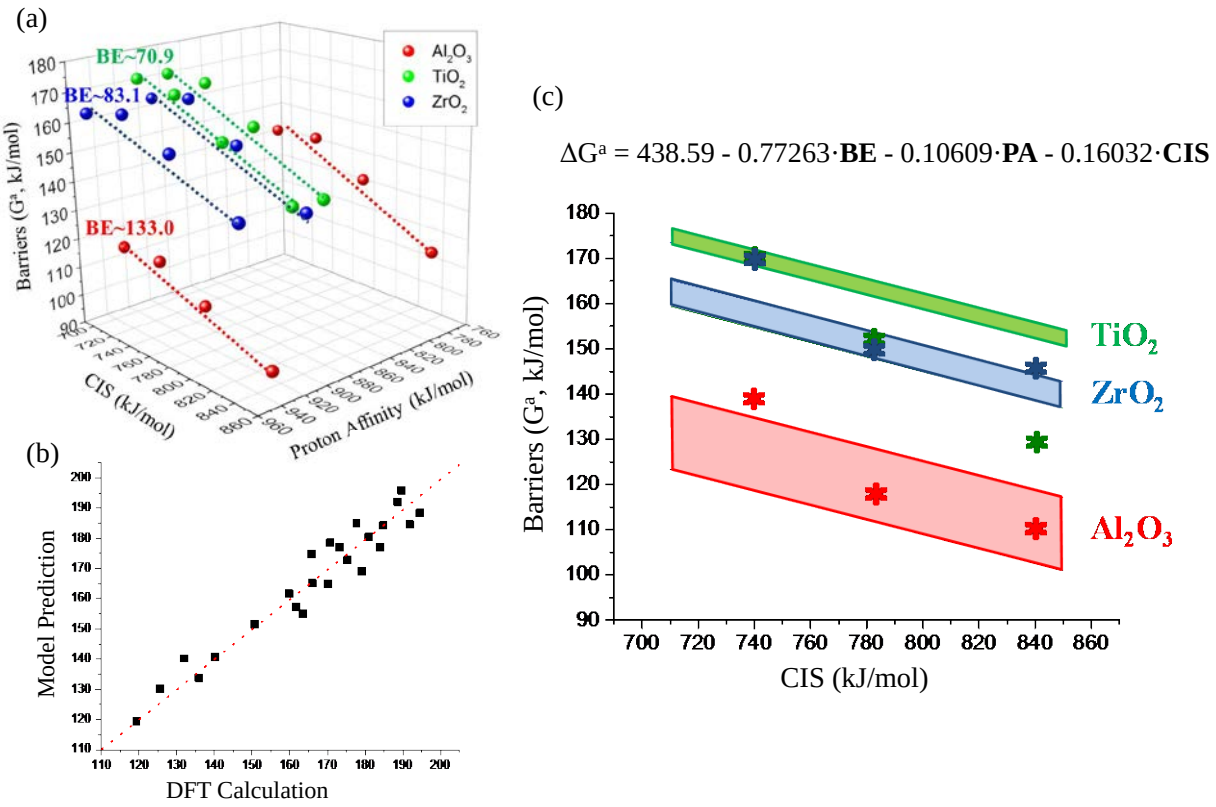


**Figure 4.** (a) Calculated Gibbs free energy dehydration barriers of the different alcohols on the oxides, as presented in Figure 4, vs. CIS of the alcohols, and proton affinity (PA of the surface-O or surface-OH. The values on the graphs demonstrate the binding energies (BE) of the alcohols on the LA site. The BE, CIS and PA are exothermic energy values (negative) and we show their absolute values in the graph. (b) Parity graph of the model-predicted vs. the DFT calculated dehydration energies. (c) Dehydration free energy barriers predicted by the developed theoretical model (colored areas) and TPD experimental barriers (asterisks) vs. CIS of the alcohols. The model is a 3-parameter linear expression describing the dehydration (free energy) barriers as a function of BE, PA and CIS. Color code: $TiO_2$-green, $ZrO_2$-blue and $\gamma$-$Al_2O_3$-red.

### 2.2.2 Descriptor-Based Alcohol Dehydration SARs

We were able to show an interplay between the type of the alcohol (CIS), the strength of the Lewis acid (BE of alcohols) and the strength of the Lewis base center (PA) in determining the overall dehydration barriers. As all these dependencies are linearly correlated, we fitted all these data with a 3 parameter linear expression that relates the dehydration free energies with the BE, the CIS and the PA. To assess the performance of the model, we compare dehydration predictions with activation energies obtained from TPD experiments in Figure 4(c). The colored boxes demonstrate the model-predicted dehydration barrier energy areas, whereas the asterisks, the experimentally observed TPD dehydration barriers. The upper limit of the boxes corresponds to PA of the hydroxyl groups, whereas the lower limit to the PA of the bridge-O groups. It should be noted that the model captures very well the dehydration trends between the different oxides. In agreement with the TPD experiments, the model predicts that γ-$Al_2O_3$ is a better dehydration catalyst than $TiO_2$ and $ZrO_2$, with the latter two oxides showing very similar dehydration activity. In addition, the model can also quantify with good accuracy the alcohol dehydration barriers.

In summary, using first-principles calculations we investigated the dehydration of different alcohols on $TiO_2$, $ZrO_2$ and γ-$Al_2O_3$. Our results demonstrate that γ-$Al_2O_3$ is a more active dehydration catalyst than $TiO_2$ and $ZrO_2$, with the latter two oxides exhibiting similar dehydration activity. Our work also demonstrates that the dehydration occurs through an E2 mechanism involving LA sites and surface O and/or OH groups of the oxides. Our results show that the OH groups act as basic centers and do not exhibit Brønsted character in the dehydration reactions. We revealed correlations between rate-limiting reaction barriers and key properties of

the oxides and the reacting alcohols. Based on these relationships, we constructed a dehydration model that uses as input the BE of the alcohols on the oxide metal centers, the proton affinity of the surface oxygen or hydroxyl groups (PA) and the CIS of the alcohols. The model developed in this work could be used to screen catalyst/alcohol systems that exhibit similar fundamental properties. Most importantly we propose a structure-activity model that is able to capture alcohol dehydration trends on different oxides as a function of system properties.

# 3.0 STRUCTURE-ACTIVITY RELATIONSHIPS IN THE PRODUCTION OF OLEFINS FROM ALCOHOLS AND ETHERS: A FIRST-PRINCIPLES STUDY

The content of this chapter is taken in part from P. Kostetskyy and G. Mpourmpakis, "Structure-Activity Relationships in the Production of Olefins From Alcohols and Ethers: A First-Principles Theoretical Study", *Catal. Sci. Technol.*, **2015**, 5, 4547-4555[66]

## 3.1 COMPUTATIONAL METHODS

As shown in Figure 1, olefin formation can occur via direct alcohol dehydration (a) or a secondary catalytic loop in which ether decomposition occurs (b) to form an additional olefin molecule. In this work, olefin formation pathways on LA sites of $Al_2O_3$, $Ga_2O_3$ and $In_2O_3$ were investigated using DFT. We focused on olefin formation pathways through i) direct alcohol dehydration of ethanol, 1-propanol, 2-propanol and 2-methyl-2-propanol and ii) ether decomposition on LA sites of i) alumina, ii) gallia, iii) india, iv) gallium-doped alumina and v) indium-doped alumina. We focus on catalytic sites that exhibit same structural characteristics and we change the metal component of group XIII oxides to address effect of acidity on the olefin formation barriers. The $Al_2O_3$ (Alox), $Ga_2O_3$ (Gaox) and $In_2O_3$ (Inox) oxide models were structurally identical to the $Al_8O_{12}$ cluster used by Roy et al. [5]. The oxygen atoms (12) that constitute the cluster assure that the metal atoms (8) exhibit oxidation states of +3, following the

stoichiometry of the bulk oxide (Figure 5). The sites of the clusters that participate in the reactions are the i) tricoordinated metal (LA) sites ii) tricoordinated neighbor oxygen (O3) site and iii) two-coordinated peripheral oxygen sites (O2). Recent work by Jenness et al.[11], showed that the coordination number of surface acid sites is directly related to their acidity. The adsorbate binding energies were highest when bound on stronger (less coordinated) acid sites. In turn, the calculated reaction barriers increased with the surface acid site coordination number (5 > 4 > 3). As a result, stronger alcohol adsorption to Al sites resulted in lowering the activation energy, a behavior which was captured by our alcohol dehydration model on group IV metal oxides[4].

All energy calculations were performed using the B3LYP[67-68] hybrid functional as implemented in Gaussian 09 package[70]. The 6-311G* triple-ζ basis set was used for Ga, Al, O, C, H atoms and the LANL2DZ effective core potential (ECP)-type basis set was used for In atoms [75]. Reaction pathways were mapped by scanning the potential energy surface of the reaction coordinate. The energy maximum that was found along the reaction coordinate was fully relaxed to a saddle point to locate the actual transition state. In complementarity with the previous approach we also used the Synchronous Transit-Guided Quasi-Newton (STQN) method to locate transition states. All transition states and local minima were obtained by full optimizations and verified by vibrational frequency and Intrinsic Reaction Coordinate (IRC) calculations.

## 3.2 RESULTS AND DISCUSSION

### 3.2.1 Alcohol Dehydration

For the energetically-preferred E2 mechanism, studies have shown significant C-O bond elongation (~1Å) and charge splitting at the transition state, exhibiting strong carbenium-ion characteristics[58-60]. The transition states of the concerted-E2 alcohol dehydration mechanism, involving $O^{CN2}$ and $O^{CN3}$ base sites, are presented in Figure 5.

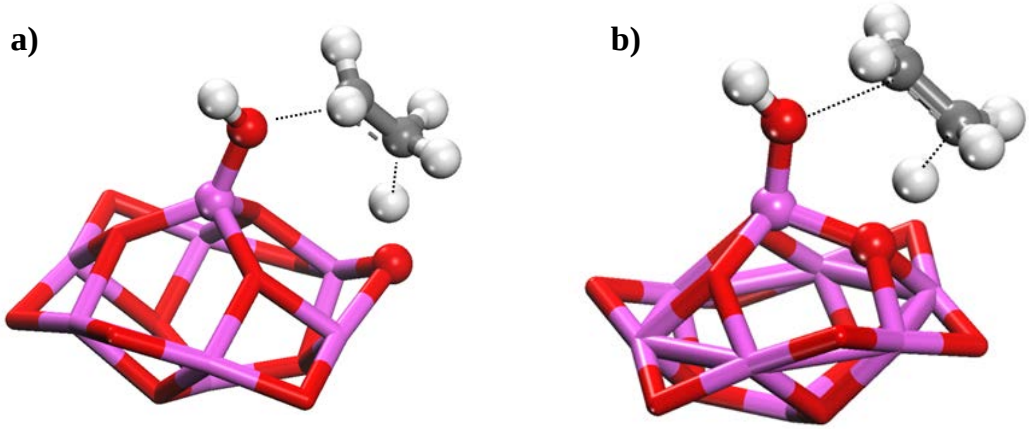


**Figure 5.** Transition states of ethanol decomposition on metal oxide catalysts involving (a) two- and (b) three-coordinated base sites via an E2 type of elimination mechanism.

In Figure 6 we present the calculated concerted-E2 dehydration barriers on the different oxides involving twofold and threefold coordinated surface oxygens (see transition states in Figure 5(a) and (b), respectively). The dehydration barriers of the different alcohols were plotted as a function CIS, exhibiting a linear correlation between the dehydration energy barriers and the CIS of reacting alcohols.

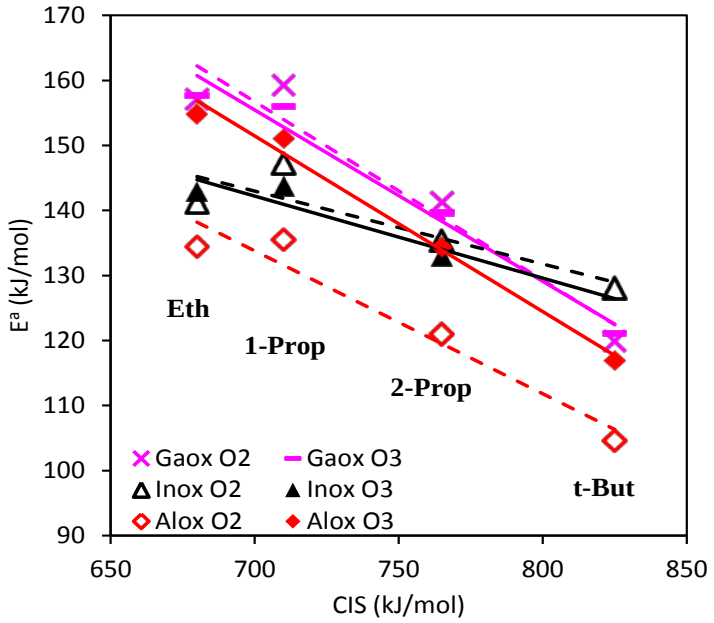


**Figure 6.** Activation energies for E2 dehydration mechanism of ethanol, 1-propanol, 2-propanol and t-butanol, as a function of their CIS involving twofold and threefold coordinated base sites (shown in open and closed symbols, respectively) for pure metal oxides (Alox, Gaox, Inox).

Alox was shown to be the most active of the three pure metal oxides in terms of dehydration energy barriers. The trends in $E_a$ vs. CIS for Alox and Gaox were nearly identical, while those observed for Inox deviated significantly in terms of the slope of the linear trend line by decreasing by a factor of 2 (Figure 6). The effect of base sites involved in the $^{\beta}H$ abstraction was only observed for Alox clusters ($\Delta E_a$ ~15 kJ/mol), whereas the difference in calculated barriers for Gaox and Inox clusters was insignificant (solid vs. dashed black and purple lines in Figure 6). It should be noted that the calculated alumina-catalyzed ethanol dehydration barriers are in excellent agreement with those calculated on smaller clusters containing twofold coordinated bridge oxygens as base sites[59].

### 3.2.2 Ether Decomposition

As shown in previously published work,[29, 36, 58] ether formation through a substitution-type reaction can compete with alcohol dehydration at low reaction temperatures. Christiansen et al.[58] investigated diethyl ether decomposition on the (100) facet of $\gamma$-$Al_2O_3$, using DFT calculations proposed a concerted ether decomposition

In the reaction scheme, shown in Figure 1(c), the first step of the ether decomposition pathway is adsorption of the reactant on the LA site, with strong interaction between the acidic metal center and the oxygen atom of the ether molecule. The second step involves a $^{\beta}H$ abstraction by basic oxygen ($O^{CN2}$/$O^{CN3}$ in our case) sites on the metal oxide. The resulting products are a weakly adsorbed alkene molecule and a stable alkoxide adsorbed on the acidic metal center of the metal cluster. Additionally, the base site involved in the decomposition reaction becomes protonated. The catalytic cycle is completed by formation of an adsorbed alcohol by recombination of the bound alkoxide to the adjacent hydrogen. Desorption of all bound species (alcohol and alkene) is the final step of the ether decomposition mechanism.

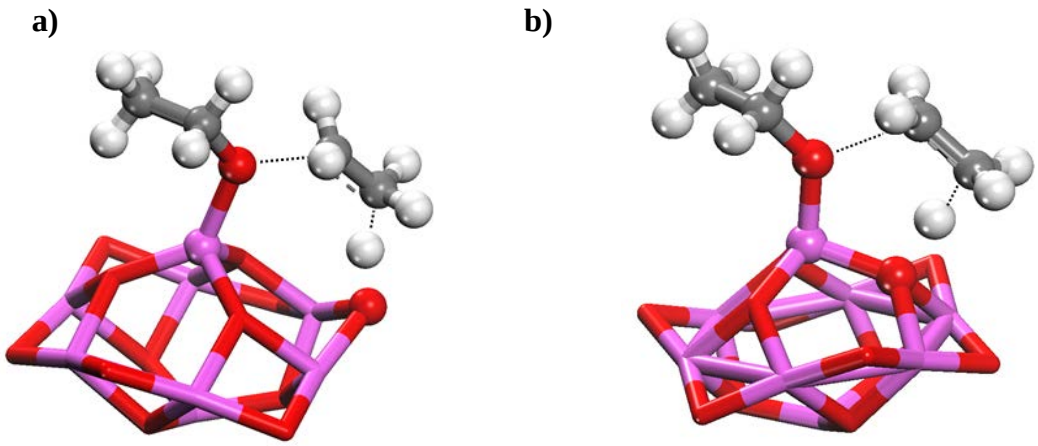


**Figure 7.** (Di-ethyl) Ether decomposition transition states on metal oxide clusters involving (a) two-dicoordinated and (b) tricoordinated oxygen surface sites.

It should be noted that alcohol dehydration to form olefins also proceeds via a concerted-E2 mechanism showing great similarities in the abstraction of $^{\beta}$H as shown in the transition states of Figure 5 and Figure 7. In addition to qualitative similarities between the aforementioned transition states involving $^{\beta}$H abstraction, a quantitative comparison can be made between the analogous reactions. In Figure 8 we plot the calculated ether decomposition barriers vs. the alcohol dehydration barriers on the different metal oxides, under the commonly observed concerted-E2 mechanism. Two key observations can be extracted from Figure 8: i) the ether decomposition barriers are strongly correlated with the alcohol dehydration barriers and ii) the ether decomposition barriers appear to be slightly higher than the alcohol dehydration barriers.

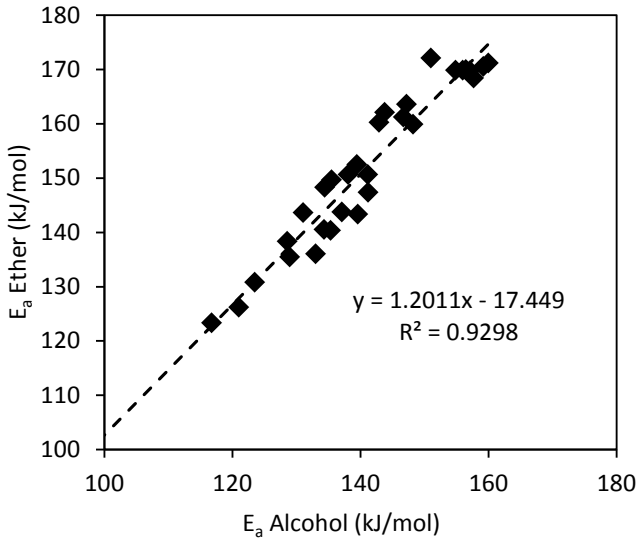


**Figure 8.** Activation energies for ether decomposition via E2-like pathway vs. alcohol dehydration via the E2 mechanism. The slope of the line (~1.2) suggests similarity between the transition states for both mechanisms, although an upward shift in barrier values is observed for ether decomposition, when compared to alcohol dehydration.

### 3.2.3 Dehydration-Decomposition Model

In our previous work on alcohol dehydration on $Al_2O_3$, $TiO_2$ and $ZrO_2$ clusters, we were able to demonstrate and quantify a relationship between the reaction barriers and LA site strength (BE of alcohols), base site strength (PA of surface oxygens) and stability of reacting of alcohol (CIS). The energetics for all reactions on all of the oxides are reported in Appendix A1 and A2 A model was constructed to predict alcohol dehydration barriers as a function of cluster properties (BE & PA) and alcohol properties (CIS), which was in excellent agreement with dehydration experiments on $Al_2O_3$, $TiO_2$ and $ZrO_2$ oxides. The analogous developed dehydration (bilinear fit) model on the mixed oxides has the form:

$$E_a = 491.52 - 0.174 \cdot PA - 0.179 \cdot BE - 0.228 \cdot CIS \quad (4)$$

Where PA, BE and CIS are model inputs of (absolute) values of proton affinity, reactant binding energy and CIS of the reacting alcohol, respectively. Detailed values of calculated BE and PA on the various clusters can be found in ref. [66]. The performance of the model is demonstrated in the parity plot of Figure 9. Although the majority of barrier values predicted by the model are within ±10 kJ/mol of those calculated (Figure 9), some deviations were observed. These deviations between model predictions and calculated energy barriers are specific to indium oxide involving the twofold-coordinated base site. The deviations are caused by the dehydration model (Equation ((4)) weighing base site PA (input variable) uniformly for all metal oxides considered, although PA sensitivity of DFT-calculated barriers is not observed in practice, resulting in under-predicted values.

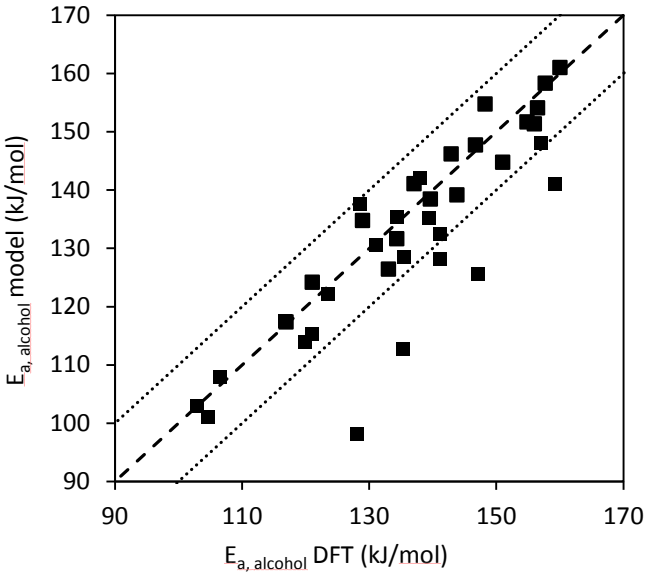


**Figure 9.** Parity plot of predicted energy barrier values and those calculated with DFT. Dashed lines represent a ±10 kJ/mol deviation range.

In the case of Alox, all of the dehydration trends observed in references [58] were found to exist in the current work: The base site strength affects the dehydration barriers and the latter decrease in an identical manner (similar slopes) as a function of the CIS of the alcohols. The alcohols were found to bind the alumina cluster the strongest, resulting in the lowest dehydration barriers among the pure metal oxides according to the dehydration model. In the case of Gaox, the higher calculated alcohol dehydration barriers (compared to Alox) are due to weaker alcohol adsorption (BE). Vimont et al. have shown that the surface acid sites present in $Ga_2O_3$ are less acidic than those of $Al_2O_3$ [52] and attributed the difference in strength to the difference in polarizing power of the cation. This difference in polarizing power (vs. $Al^{3+}$) was attributed to i) smaller charge-to-radius ratio of $Ga^{3+}$ ions and ii) smaller ionicity of the Ga-O bond. An effect of base site strength on calculated energy barriers was not observed.

Calculated energy barriers for dehydration involving the di- and tricoordinated base sites on Gaox clusters were identical (Figure 6). In the case of Inox, all of the trends observed thus far

for Alox and Gaox are at odds with those found between system properties (BE, PA and CIS) and calculated dehydration energy barriers. First, BE effects contradict those observed on gallia clusters, where alcohols bind both clusters with identical adsorption energies, with differing dehydration barriers. Second, the decrease in calculated energy barriers with respect to CIS (slope of black lines in Figure 6) was lower by a factor of 2 compared to Alox and Gaox. Finally, the effect of base site strength was not observed. A possible reason for this deviation from the model's prediction could be the fact that the average metal-oxygen bonds in indium oxide are longer than any other oxide, resulting to transition states where the intermediates are stretched.

## 3.3 CONCLUSIONS

In summary, we used DFT calculations to investigate the olefin formation pathways via direct alcohol dehydration to olefins and (corresponding) ether decomposition on LA sites of $Al_2O_3$, $Ga_2O_3$ and $In_2O_3$. Our results demonstrate that aluminum oxide catalyst is most active in alcohol dehydration reactions, compared to oxides of gallium and indium. We apply our recently proposed concept of oxide-based SARs[59], to develop a model that predicts dehydration barriers of various alcohols on mixed oxides utilizing catalyst (surface acidity, basicity) and alcohol (CIS) properties. Most importantly, we revealed a strong correlation between the energy barriers of ether decomposition and alcohol dehydration that guided us to successfully extend the dehydration model predictions to ether decomposition. Our work demonstrated systematic methods to relate different (and competing) chemistries, that exhibit transition states that are structurally similar, and develop activity models on heterogeneous catalysts.

# 4.0 IMPORTANCE OF CARBENIUM IONS IN THE CONVERSION OF ALCOHOLS

The content of this chapter is taken in part from P. Kostestkyy, J. P. Maheswari and G. Mpourmpakis, "Understanding the Importance of Carbenium Ions in The Conversion of Biomass-Derived Alcohols with First Principles Calculations" *J. Phys. Chem. C*, **2015**, 119, 16139-16147 and P. Kostetskyy and G. Mpourmpakis, "Carboranes: the strongest Brønsted acids in alcohol dehydration" *Catal. Sci. Technol.*, **2017**, 7, 2001-2011.[76-77]

## 4.1 INTRODUCTION

Acid catalysts of different types, such as Brønsted (e.g. zeolites) and Lewis (e.g. metal oxides such as $\gamma$-$Al_2O_3$), have been shown to be active for alcohol dehydration reactions[27-28, 36, 59-60, 65-66]. The nature of the acid site (i.e. Lewis vs. Brønsted) can influence the type of reaction mechanism[76]. Both Lewis and Brønsted acid-catalyzed alcohol dehydration reactions involve transition states with carbenium ion characteristics[27, 59]. A carbocation is an ion with positive charge on a carbon atom with a vacant p-orbital[78]. Carbocations are classified based on the number of valence electrons in the charged carbon atom. For instance, carbocations with three valence electrons are referred to as carbenium ions, whereas, structures with five or six valence electrons are classified as carbonium ions[78-79]. The carbenium ion structures resemble $sp^2$

hybridization with a trigonal planar molecular geometry. They exhibit rearrangements[80], resonance[81], and hyperconjugation[82] to distribute the positive charge and stabilize the final structure. CIS follows a trend of the primary heteroatom substitution: primary < secondary < tertiary. CIS can be quantitatively expressed in terms of the gas phase PA of the corresponding alkene to form the carbenium ion (Equation (1))[60].

Carbocations are key intermediates in Brønsted and Lewis acid-catalyzed alcohol dehydration reactions. Dehydration of alcohols on γ-alumina, catalyzed by LA sites as suggested by Roy et al.[60], shows a linear correlation between the dehydration activation energy and the CIS. Similarly, work of Gorte et al.[27] on Brønsted acid catalysts shows a linear trend in the heat of formation of the adsorption complex on the catalyst surface and the PA of adsorbates like alcohols, pyridines, amines and nitriles. In addition, Janik et al. studied the alcohol dehydration on polyoxometalates and showed that the reaction barriers are linearly related with the catalyst deprotonation energy (measure of acid strength) and inversely related with the alcohol PA (base strength)[83]. As a result, the dehydration of alcohols involves transition states with carbenium ion characteristics, highlighting the importance of CIS as a quantitative descriptor that determines both the activity and selectivity in the dehydration of alcohols[27, 59-60, 84].

In this work, we employed high-level ab-initio theoretical methods to investigate the effect of molecular structure on the physicochemical properties of a set of alcohols (reactants) that appear to control dehydration chemistry. Specifically, we calculated the CIS – alkene binding $H^+$ and PA - alcohol binding $H^+$ of various C2-C8 alcohols, to show the effect of alcohol size and degree of primary heteroatom substitution on the properties of the reactive species.

## 4.2 COMPUTATIONAL METHODS

We employed various levels of ab-initio calculations, namely, B3LYP combined with the 6-311G* basis set [67], CBS-QB3 [85] and G4 [86] theory as implemented in the Gaussian 09[70] computational package. Structures of C2-C8 species, including alcohols, protonated alcohols, carbenium ions (protonated alkenes) and alkenes, were fully optimized and the ground states were verified by the absence of any imaginary frequencies. The total (gas phase) Gibbs free energies and enthalpies were calculated at the standard state of T = 298.15 K and P = 1 atm.

We have accounted for all alcohol isomer structures in the C2-C6 size range and representative alcohols (primary, secondary, tertiary - including cyclic) from C7 and C8 alcohols (total of 42 alcohols). The CIS is calculated in terms of PA of the alkene according to (5):

$$CIS = PA_{alkene} = |H_{carbenium\ ion} - H_{alkene}| \quad (5)$$

Where $H_{carbenium\ ion}$ and $H_{alkene}$ are the total enthalpies of the carbenium ion and the alkene, respectively [60]. Similarly, we can calculate the free energy change in the CIS as ($CIS = G_{carbenium\ ion} - G_{alkene}$). In both cases it has been assumed that the free energy and enthalpy of the proton is zero.

The PA of the alcohol ((6)) can be defined as the enthalpy (or free energy) change between the protonated and non-protonated alcohol states.

$$PA_{alcohol} = |H_{protonated\ alcohol} - H_{alcohol}| \quad (6)$$

The Gibbs free energy (and enthalpy) of the dehydration reaction (Equation (7)) for the various alcohols were calculated using (8).

$$C_nH_{2n+1}OH \rightarrow C_nH_{2n} + H_2O \quad (7)$$

$$\Delta G_{rxn} = G_{alkene} + G_{water} - G_{alcohol} \quad (8)$$

The protonated alcohol can be considered as a carbenium ion (CI) stabilized by a water molecule. The binding free energy (BE) of water on the adjacent CI for the protonated alcohols was calculated according to Equation (9).

$$BE_{H_2O} = G_{protonated\ alcohol} - G_{carbenium\ ion} - G_{water} \quad (9)$$

We can further analyze this relationship by describing the BE as a function of the CIS (calculated in terms of free energy differences) by using equations 1 and 2 as follows:

$$G_{protonated\ alcohol} = PA_{alcohol} + G_{alcohol} \quad (10)$$

$$G_{carbenium\ ion} = CIS + G_{alkene} \quad (11)$$

Substituting equations 10 and 11 into 12, we obtain:

$$BE_{H_2O} = PA_{alcohol} + G_{alcohol} - CIS - G_{alkene} - G_{water}$$

$$BE_{H_2O} = PA_{alcohol} - CIS - \Delta G_{dehydration} \quad (12)$$

As shown in equation (12), $BE_{H_2O}$ can be expressed in terms of alcohol CIS, PA and the net free energy change of the dehydration reaction. This is particularly interesting, as it combines multiple key properties of the species involved in alcohol dehydration into a simple algebraic expression. Please note that CIS and the PA values were highly exothermic, but for ease of analysis, absolute values of both CIS and PA were reported.

All transition states in reaction pathways were located by scanning the potential energy surface along the reaction coordinate. The energy maximum that was found along the reaction coordinate was fully relaxed to a saddle point to locate the actual transition state. Transition states (TS) were verified both by the presence of a single imaginary frequency and Intrinsic Reaction Coordinate (IRC) calculations[87] at the B3LYP/6-311G* level of theory[67, 85]

## 4.3 RESULTS AND DISCUSSION

### 4.3.1 Carbenium Ion Stability versus Proton Affinity

When examining the stability of the protonated alkenes (CIS), we observed a higher number of hyper-conjugative structures for more substituted alcohols (i.e.: tertiary > secondary > primary). In addition, a high inductive effect (+I) from alkyl groups adjacent to the primary carbon atom was observed in the same order, resulting in delocalization and stabilization of the positive charge, making the protonated alkene more stable.

In Figure 10 we have plotted CIS vs. PA for a range of alcohols of varying substitution, highlighting the alcohols as a function of degree of alcohol substitution (primary, secondary, tertiary). The PA and CIS values are both exothermic and their difference decreases as a function

of degree of substitution (Figure 10). The most interesting feature of Figure 10 is that the protonation of a hydroxyl group of an alcohol (to form a water-stabilized carbenium ion) is preferred (more exothermic) to the protonation of the olefin to form the corresponding carbenium ion. This is the case in the formation of primary and secondary carbenium ions, whereas, it becomes indifferent (PA=CIS) for the formation of tertiary carbenium ions – purple points fall on the axis x=y on Figure 10.

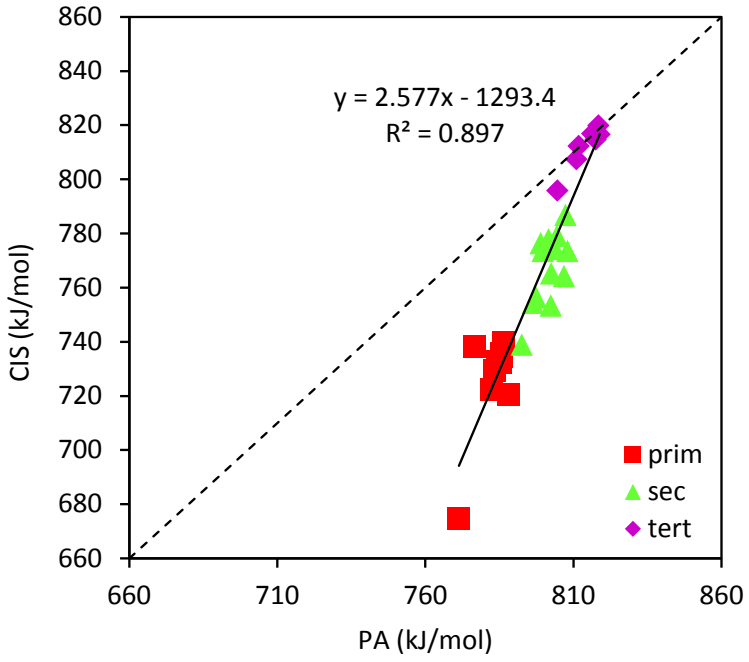


**Figure 10.** CIS vs. PA for primary (red squares), secondary (green triangles) and tertiary (purple rhombs) alcohols, calculated using the G4 method (the dotted line shows the y=x).

All the relationships demonstrated so far have been derived based on thermodynamic calculations. The results showed a strong linear correlation between the CIS and PA. Both properties (CIS and PA) increase with the degree of alcohol substitution (tertiary > secondary >

primary). In addition, we showed that the CIS and the PA of the alcohols can be interchangeably used as descriptors in both Lewis and Brønsted catalyzed dehydration mechanisms.

In addition, we were able to demonstrate that the stability of the formed carbenium ions play a key role on the kinetics of dehydration reactions. As stated previously, the preferred mechanism in the Lewis catalyzed alcohol dehydration on $\gamma$-$Al_2O_3$ is the concerted E2 mechanism. In Figure 11 we expanded this trend to the $Al(OH)_3$, a LA catalyst, and, most importantly to sulfuric acid, which is a Brønsted acid (BA) catalyst – shown to favor a concerted intramolecular elimination pathway. We relate the calculated activation energies with the (a) CIS and (b) PA of the different alcohols for the energetically-preferred pathways in LA- and BA-catalyzed alcohol dehydration reactions.

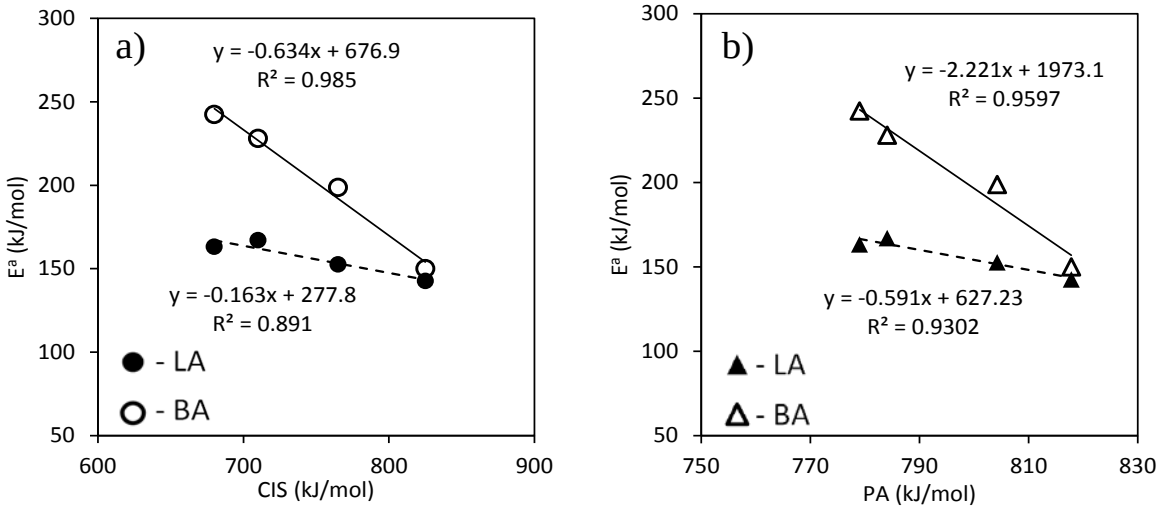


**Figure 11.** Brønsted (BA) and Lewis acid (LA) catalyzed activation energies of ethanol, 1-propanol, 2-propanol and t-butanol, as a function of (a) CIS and (b) PA calculated at the B3LYP/6-311G* level of theory. Linear trends are observed in every case.

The calculated activation energies were shown to correlate linearly both with the CIS and the PA, clearly capturing the effect of alcohol substitution on the corresponding reaction barriers and are represented by a negative slope of the line. The strong linear correlations are due to the fact that both the Brønsted and the Lewis mechanisms have transition states that exhibit carbenium ion characteristics. Calculated partial charge of the CI in ethanol dehydration were +0.51 and +0.83 |e-| in the Lewis- and Brønsted acid-catalyzed transition states, respectively. The reason that these reactivity descriptors (CIS and PA) could be interchangeably used (see Figure 11 (a) and (b)) is based on the strong linear correlation between the two, shown in Figure 10. An important observation in Figure 11 is that the Brønsted catalyzed dehydration mechanism showed a higher slope and dependence on the type of the alcohol, than the Lewis catalyzed mechanism. Figure 11 shows that although the Lewis-catalyzed dehydration mechanism – at least on these catalysts – is energetically preferred, the Brønsted catalyst can achieve higher dehydration selectivities (higher slopes).

### 4.3.2 Trends in Acid Catalyzed Alcohol Dehydration

The correlations between calculated dehydration activation energies and alcohol CIS/PA show linear trends, and these correlations can be quantified in terms of the slope of $E_a$ vs. CIS line. Recent work has demonstrated a linear relationship for alcohol dehydration reactions on several LA catalysts[59-60, 66, 76, 88], evolving via a concerted E2-type mechanism that is characterized by strong CI character at the transition state. In addition, alcohol dehydration catalyzed by strong Brønsted acids has recently[88] been shown to evolve via a concerted intramolecular mechanism, characterized by a simultaneous C-O/C-H cleavage and a high degree of charge separation at the transition state, forming carbenium ion (CI) intermediates. Based on these commonly observed

characteristics, we compare the dehydration performance of some BA and LA catalysts in terms of calculated activation energies vs. CIS in Figure 12.

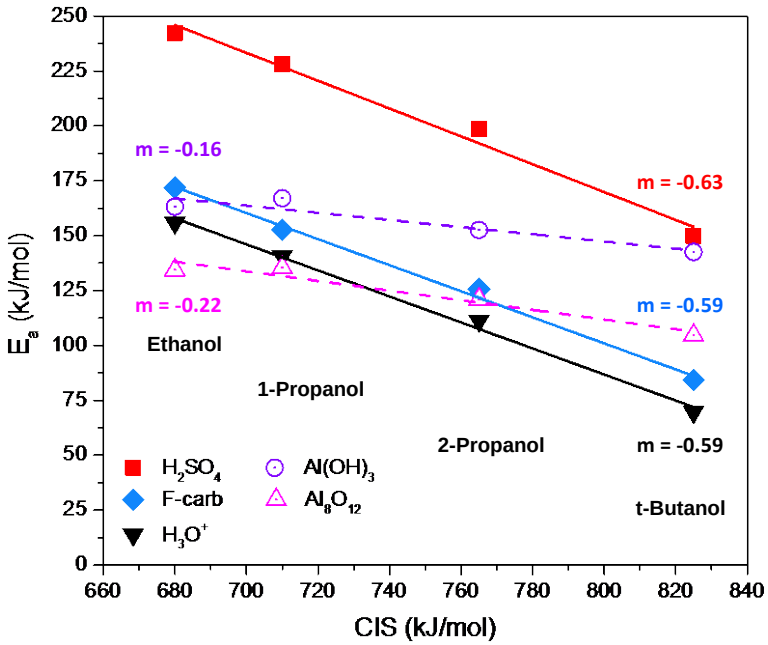


**Figure 12.** Activation energies vs. CIS for Brønsted and Lewis acid catalysts evolving through concerted (intramolecular and E2) reaction mechanisms. Slopes of linear fits (from y = mx +b) reported for each acid catalyst and correspond to the colors of individual lines.

A total of five different acids were chosen for comparison: two representative cluster models of aluminum oxide ($Al(OH)_3$) and γ-$Al_2O_3$ ($Al_8O_{12}$)[66, 76], and three Brønsted acids ($H_2SO_4$, F-Carb and $H_3O^+$) , all catalyzing the dehydration reactions of ethanol, 1-propanol, 2-propanol and t-butanol. The primary differences in the observed trends between BA- and LA-catalyzed reactions lie in the slope of $E_a$ vs. CIS, as shown in Figure 12. Specifically, the greater slopes correspond to the BA catalysts (~ -0.6), being significantly larger in magnitude (factor of 3) when compared to those corresponding to (LA) aluminum oxides (~ -0.2).

The magnitude of CIS dependence is directly related to the mechanism of olefin formation (intramolecular elimination vs. E2), which in turn governs the extent of CI character in the transition state. The greater charge separation observed in the intramolecular Brønsted-catalyzed transition states relative to those in Lewis-catalyzed E2 mechanism on oxide surfaces is significant, suggesting that the stability of the carbenium ion intermediates play a significant role in the mechanism. For example, the calculated partial charge of the (ethanol) CI in the transition state for alumina-catalyzed dehydration reaction (+0.54) was significantly lower when compared to the Brønsted acids (+0.83 – 0.89).

The existence of CI intermediates in acid-catalyzed reactions have allowed us to identify and propose either the PA or the CIS as interchangeable alcohol (dehydration) reactivity descriptors for both LA and BA catalysis. Now we reveal that the $E_a$ vs. CIS dehydration slopes between alcohols of different substitution can potentially reveal the dehydration reaction mechanism (intramolecular vs. E2). This observation is very important since experimentalists can now perform dehydration experiments of two differently-substituted alcohols (e.g. primary and secondary) and from the dehydration slope ($E_a$ vs. CIS) identify the potential intramolecular $^{\beta}$H elimination vs. E2 mechanism. For example, a linear dependence of experimental activation barriers (via the E2 mechanism) vs. CIS for primary, secondary and tertiary alcohols was shown by Roy et al.[60], with a calculated slope of -0.25. These reactant-type alcohol descriptors (CIS and PA) as well as the dehydration slopes can be used to screen activity and selectivity trends between different alcohols in acid-catalyzed chemistry (both Brønsted and Lewis).

## 4.4 CONCLUSIONS

Alcohol PA and CIS are interchangeable reactant-side stability descriptors as both are a function of structural and electronic properties of the reactants. Alcohols are known to dehydrate on solid acid catalysts via several surface mechanisms, in which they exhibit varying degrees of CI character. We demonstrate a dependence of the dehydration slopes presented in this work ($E_a$ vs. CIS) to the degree of CI character in alcohol dehydration reactions, which in turn, depends on the reaction mechanism. Thus, by experimentally calculating dehydration slopes with the use of two alcohols of different substitution, one can get evidence about the reaction mechanism (intramolecular or E2) in both LA- and BA chemistries. These retrieved relationships are especially relevant to the field of solid acid catalysis, a widely-studied area with a vast range of industrial applications, including the formation of olefins (polymer building blocks) from biomass-derived alcohols as well as fuels and chemicals from sugars and polyols.

# 5.0 DESIGN OF SELECTIVE ETHANOL DEHYDRATION CATALYSTS FOR ETHYLENE PRODUCTION

The content of this chapter is taken from: N. Austin, P. Kostetskyy and G. Mpourmpakis, "Design of Highly Selective Ethanol Dehydration Nanocatalysts for Ethylene Production", *Nanoscale*, **2018**, 10, 4004-4009.

## 5.1 INTRODUCTION

Earth-abundance and low cost of plant biomass make it a viable substitute to fossil fuels as a carbon-neutral feedstock for production of fuels and chemicals.[6] Generally, high oxygen content is an issue in the field of biomass processing, forming a range of alcohols, polyols and phenols with one or more hydroxyl (OH) functionalities. The high oxygen content of these biomass products has been shown to lower the overall value and cause processing complications.[6, 89-91] Unit operations to reduce oxygen content of biomass products are important for improving overall efficiency and process economics. Catalytic upgrading of oxygenates is a vital component in biomass processing operations, characterized by cleavage of oxygenate C-O bonds. Dehydration of aliphatic alcohols via acid-based catalysis is an important, industrially-relevant reaction. Solid acids, including metal oxides, zeolites, and polyoxometalates, have been shown to be active alcohol dehydration catalysts.[27, 58-60, 92] Dehydration reactions occur at

moderate temperatures (~500 K) and proceed via unimolecular and bimolecular pathways, forming olefin and ether products.[29, 58, 63-64, 93] The formation of acetaldehyde (via dehydrogenation reactions) should not be expected in these catalytic systems, as it has been shown in recent computational[9] and experimental[13] studies that for γ-$Al_2O_3$, which exhibits undercoordinated, Lewis surface acid sites, the formation of ethers and olefins is majorly preferred over aldehydes. Ethylene and diethyl ether (DEE) are ethanol dehydration products and precursors in the production of polymers, solvents, fuels, and specialty chemicals.[90-91] Solid acid catalysts currently used for alcohol dehydration are generally limited in selectivity control therefore requiring the tuning of operating conditions.[64, 93] The design of highly stable, selective and active heterogeneous catalysts is the "Holy Grail" in catalysis and in processes of industrial relevance, such as the dehydration of ethanol to ethylene (polymer building block).

LA and BA catalysts are active in alcohol dehydration to olefins, with the preferred reaction mechanism being primarily a function of nature of active site and substitution of the reacting alcohol.[76] Both LA- and BA-catalyzed dehydration reactions are characterized by formation of carbenium ion (CI) intermediates in the rate-determining steps of the reaction pathway.[27, 60, 76] γ-$Al_2O_3$ has been shown to be one of the strongest among acidic oxides.[59, 66] The coordination environment of alumina surface sites plays a key role in the catalyst reactivity. Recent computational work has shown the tricoordinated aluminum sites ($Al^{CN3}$) to be most acidic[61, 66] and has been shown to exist on the (110) surface terminations of γ-$Al_2O_3$[37, 94-95].

The two reaction pathways for alcohol dehydration (DEE vs. ethylene) compete in selectivity at moderate reaction temperatures.[64, 93] The selectivity towards the ether pathway increases at lower temperatures and higher reactant pressures. In addition, selectivity has also been shown to be a function of alcohol chain length and substitution, preferring olefin formation

with more substituted species – i.e. more stable carbenium ion intermediates. Specifically, Kang et al.[64] reported a ~90% olefin selectivity increase from ethanol to isobutanol at identical reaction conditions, indicating that molecular structure of reactants as well as surface sites strongly affect the observed rates. Among this complexity, we pose a question: can we design active and selective catalysts that exhibit high olefin selectivity? Specifically, the goal is to design a catalyst capable of preferentially catalyzing the ethylene route. To the best of our knowledge, this work is the first to show rational design of mixed metal-oxide-protected metal nanocluster catalysts with structure-based selectivity towards the olefin pathway. Specifically, we demonstrate that one can take advantage of the high curvature of nanoparticles, stabilized by metal oxide complexes with generated acid sites apart from each other that do not favor bimolecular reactions, responsible for ether production.

## 5.2 COMPUTATIONAL METHODS

Alcohol dehydration towards olefin and ether formation was investigated on tri-coordinated Lewis acid sites of metal oxides $XO_3$, (X=Al, Ga, and In), stabilized on $M_{13}$ icosahedral (initially) clusters (M=Ag, Au, Cu). The structure of the optimized $M_{13}X_4O_{12}$ nanoclusters are shown in Figure 13. Systems composed of metal oxides supported on transition metals have been successfully used to investigate industrially relevant reactions such as CO oxidation and the water gas shift reaction (WGS).[96-99] We investigated the structural, electronic and catalytic properties of these nanoclusters (9 in total) using the BP86 functional[100-101] combined with the def2-SV(P)[102] basis set and the resolution of identities (RI) technique[101, 103-104] as implemented in Turbomole 6.6. For the reaction mechanisms studied, all transition states and local minima were

verified with frequency calculations. Key reaction paths were calculated at the B3LYP[67-68, 105] level of theory (hybrid density functional). Cohesive energy and free energy of formation calculations were performed to assess the stability of the nanoclusters. Equation (13) was used to determine the cohesive energy (BE per atom (n)) of the nanoclusters:

$$BE/29 = [E(M_{13}X_4O_{12}) - 13\times E(M) - 4\times E(X) - 12\times E(O)]/29 \quad (13)$$

The cohesive energy quantifies the average bond strength, and thus, the stability, of the atoms forming the $M_{13}X_4O_{12}$ nanoclusters. The stability of the nanoclusters was also assessed with free energies of formation (Equation (14)) calculated according to the following chemical reaction: $4Al(OH)_3 + M_{13} \rightarrow M_{13}Al_4O_{12} + 6H_2$:

$$\Delta G_f = G(M_{13}X_4O_{12}) + 6\times G(H_2) - G(M_{13}) - 4\times G(X(OH)_3)] \quad (14)$$

Where $G(M_{13}X_4O_{12})$, $G(H_2)$, $G(M_{13})$, and $G(X(OH)_3)$ are the free energies of an isolated $M_{13}X_4O_{12}$ nanocluster, an $M_{13}$ nanocluster, a $H_2$ molecule, and a $X(OH)_3$ molecule, respectively.

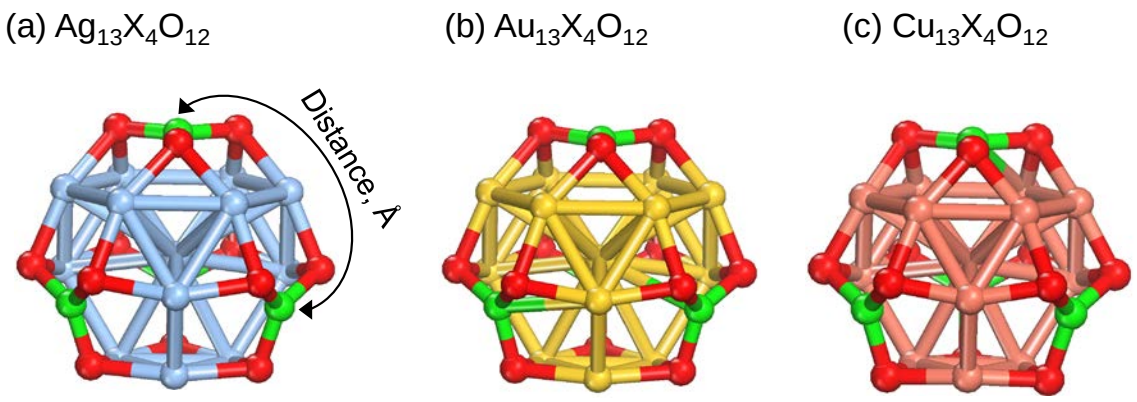


**Figure 13.** Structural representations of (a) $Ag_{13}X_4O_{12}$, (b) $Au_{13}X_4O_{12}$ and (c) $Cu_{13}X_4O_{12}$ nanoparticles. Where "X" (green atoms in the structures) for each chemical formula can be Al, Ga, or In. The approximate distance between each metal oxide center "X" is 5.4 Å, 5.0 Å, and 5.0 Å for Ag, Au, and Cu respectively.

## 5.3 RESULTS AND DISCUSSION

### 5.3.1 Nanocatalyst Stability Assessment

The stability of the $M_{13}X_4O_{12}$ nanoclusters is shown in Figure 14 and quantified in terms of cohesive energy (CE) as a function of $M_{13}X_4O_{12}$ nanocluster composition. The $Cu_{13}Al_4O_{12}$ nanocluster was determined as the most stable nanocluster with a CE of -101.52 kcal/mol (negative values represent exothermicity). Furthermore, within each metal type we determined that the $M_{13}X_4O_{12}$ nanoclusters containing aluminum (X=Al) were the most favorable structures. We have previously shown that the cohesive energy of $M_6$ (Ag, Au, Cu) clusters follows the trend (in kcal/mol): $|CE_{Cu} = -84.35| > |CE_{Au} = -34.68| > |CE_{Ag} = -27.64|$.[106] The observed CE trend in this current work is reversed for Au and Ag in $M_{13}Al_4O_{12}$: ($|CE_{CuAl/Ga/In}| > |CE_{AgAl/Ga/In}| > |CE_{AuAl/Ga/In}|$). However, just as with our previous work, the difference in CE values between Ag and Au (~2 kcal/mol difference) is not as significant as the difference between Ag/Au and Cu

(~22 kcal/mol difference). Due to the stability of $M_{13}Al_4O_{12}$, we selected these clusters for analysis of the alcohol dehydration reactions to ether and olefin products. Specifically, we investigated the dehydration of ethanol to form ethylene via the concerted (E2) and sequential (Intramolecular – Intra.) mechanisms, and formation of DEE via the (competing) $S_N2$ substitution reaction.

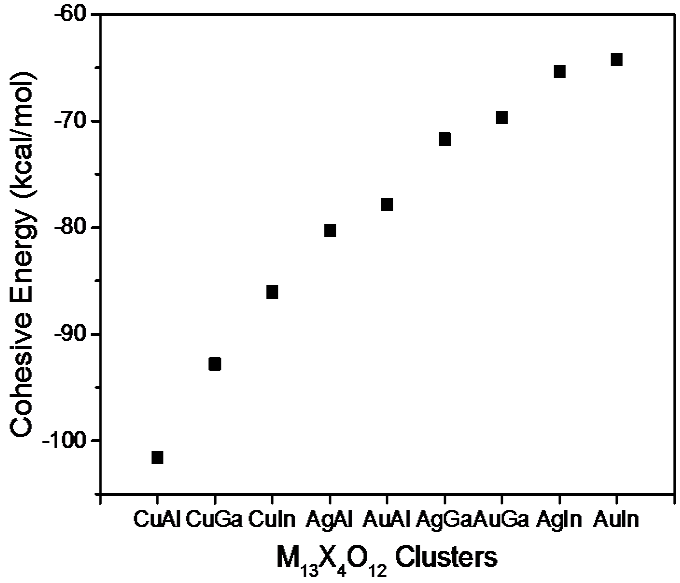


**Figure 14.** Cohesive energy of the $M_{13}X_4O_{12}$ clusters where M=Ag, Au, or Cu and X=Al, Ga, or In. The x-axis is abbreviated showing the MX combinations.

The use of these potentially highly selective nanoclusters in catalysis relies on their feasibility to be synthesized in the lab. Thus, to verify the synthesis potential of our novel nanocatalysts, we performed free energy of formation calculations at 500 K (represents the typical operating condition in alcohol dehydration reactions) on the synthesis of the $M_{13}Al_4O_{12}$ nanoclusters, using Equation (14).

We calculated the formation free energies of all three clusters and found that the energies followed the trend: $\Delta G_{Cu}$ (-148.1 kcal/mol) < $\Delta G_{Ag}$ (117.8 kcal/mol) < $\Delta G_{Au}$ (232.4 kcal/mol).

This formation energy trend follows what has been reported for $CeO_x$ particles supported by Au(111), Ag(111), and Cu(111).[107] Our results showed that the most stable (most negative CE) catalyst in our study, the $Cu_{13}Al_4O_{12}$ system, was the most thermodynamically favored, while the formation of $Au_{13}Al_4O_{12}$ and $Ag_{13}Al_4O_{12}$ was thermodynamically uphill. The $Cu_{13}Al_4O_{12}$ system, in addition to being a very active and selective alcohol dehydration catalyst, has the potential of being synthesized according to our thermodynamic analysis. It should be noticed that these metal-oxide-protected metal nanoclusters resemble the thiolate-protected metal nanoclusters. For example, the experimentally synthesized $Au_{25}(SR)_{18}$ nanocluster[108] consists of a 13-atom metal core, stabilized by a thiolate shell network, exhibiting 12 contacts with the core[109]. Similarly, in our work the $M_{13}Al_4O_{12}$ nanoclusters, consist of a 13-atom metal core, protected by an oxide shell that makes 12 contacts (O-bonds) with the core.

### 5.3.2 Catalytic Performance in Alcohol Dehydration

Figure 15 illustrates the reaction energy profiles for E2 and intramolecular (Intra.) mechanisms on the $M_{13}Al_4O_{12}$ clusters for ethanol dehydration to ethylene. In recent publications the E2 mechanism has been shown to be preferred for alcohol dehydration over the sequential intramolecular pathway on LA sites,[59] with the C-$^{\beta}$H bond cleavage being rate-limiting in both mechanisms. Identically, we also found the sequential mechanism to exhibit significantly higher activation barriers (state V in Figure 15) for the abstraction of a hydrogen atom from the β-carbon. As a result, we will focus on the E2 reaction mechanism as dominant on $M_{13}Al_4O_{12}$ clusters for the remainder of this work.

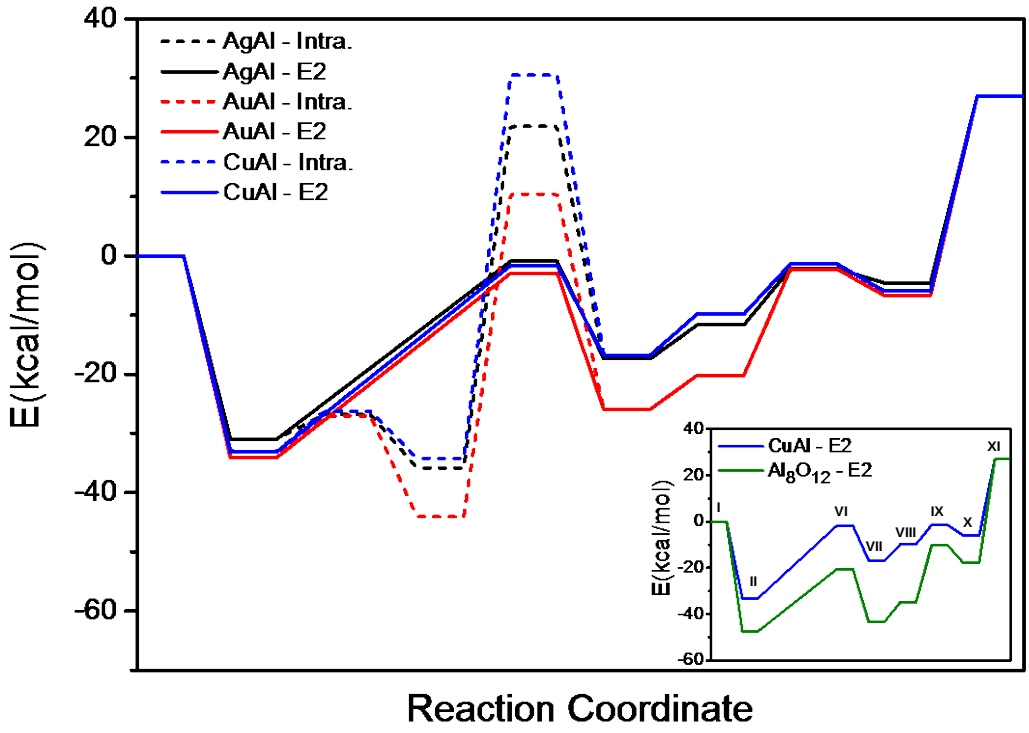


**Figure 15.** Reaction pathways for ethanol dehydration on $Ag_{13}Al_4O_{12}$, $Au_{13}Al_4O_{12}$, $Cu_{13}Al_4O_{12}$ via the sequential (Intra.) and concerted (E2) reaction mechanisms. The roman numerals on each step represent: I. Reference state with gas-phase molecular nanocluster and ethanol in infinite separation, II. ethanol adsorption, III. TS1 in Intra. Mechanism with O-H bond dissociation, IV. ethoxide formation, V. TS2 in Intra. mechanism of ethylene formation, VI. TS for E2 concerted mechanism of ethylene formation, VII. physisorbed ethylene and chemisorbed dissociated water on the nanocluster, VIII. ethylene desorption, IX. TS for water formation, X. adsorbed water, and XI. final state with water desorption and the regeneration of the catalyst. The inset graph (bottom right) compares the reaction pathway for ethanol dehydration on the $Cu_{13}Al_4O_{12}$ nanocluster to that of the pure alumina systems.

The E2 activation energy barriers calculated on clusters in this work for ethanol dehydration to ethylene are comparable ($E_a$ = ~31 kcal/mol) to those previously reported for pure alumina systems, performed at the B3LYP[6, 8, 15] ($E_a$ = 32-37 kcal/mol) and PW91[58] levels of theory ($E_a$ = 37 kcal/mol). The calculated alcohol dehydration activation barriers for the sequential (Intra.) and concerted (E2) mechanisms followed the trend Au < Ag < Cu and Ag <

Au ≈ Cu in terms of core composition, respectively. The rate-limiting reaction barriers in the sequential pathway were calculated to be 57.66, 54.51, and 64.72 kcal/mol, while those in the E2 pathway were calculated to be 29.98, 31.08, and 31.43 kcal/mol, on Ag-, Au-, and Cu-based nanoclusters, respectively. In the inset graph located at the bottom right of Figure 15 (solid green line: $Al_8O_{12}$ and solid blue line: $Cu_{13}Al_4O_{12}$), we compare the ethanol dehydration pathway on the $Cu_{13}Al_4O_{12}$ nanocluster (the most stable nanocluster from our CE calculations) to the pure alumina cluster ($Al_8O_{12}$, see references 8 and 15), with both systems exhibiting strong Lewis (tricoordinated) Al sites and treated at the BP86 level of theory. As shown in the inset of Figure 15, the E2 activation energies of the pure alumina system (26.88 kcal/mol) is lower than that on the $Cu_{13}Al_4O_{12}$ nanocluster. Although the pure alumina systems bind alcohol (-47.37 kcal/mol) and water (-44.79 kcal/mol) stronger, which contributes to decreasing the dehydration barrier as a result of the recently identified SARs in LA-catalyzed alcohol dehydration reactions[59, 66], this strong binding leads to eventual deactivation of the catalyst by water poisoning[17,18] (Sabatier principle). Due to the weaker interactions between the $Cu_{13}Al_4O_{12}$ nanocluster and ethanol (-33.08 kcal/mol) and water (-32.91 kcal/mol), less energy would be required to regenerate the bare $Cu_{13}Al_4O_{12}$ nanocluster, compared to the pure alumina analogue, making it a more active and robust alcohol dehydration catalyst. Figure 16 shows the optimized geometries of elementary steps involved in the reaction mechanism for alcohol dehydration to ethylene on the $Cu_{13}Al_4O_{12}$ nanocluster. To further address the reaction energy profiles for ethylene formation on the $Cu_{13}Al_4O_{12}$ nanocluster compared to the pure alumina system, we repeated the calculations using the hybrid B3LYP functional. We found that the results generated using the B3LYP functional agreed very well with the observations at the BP86 level.

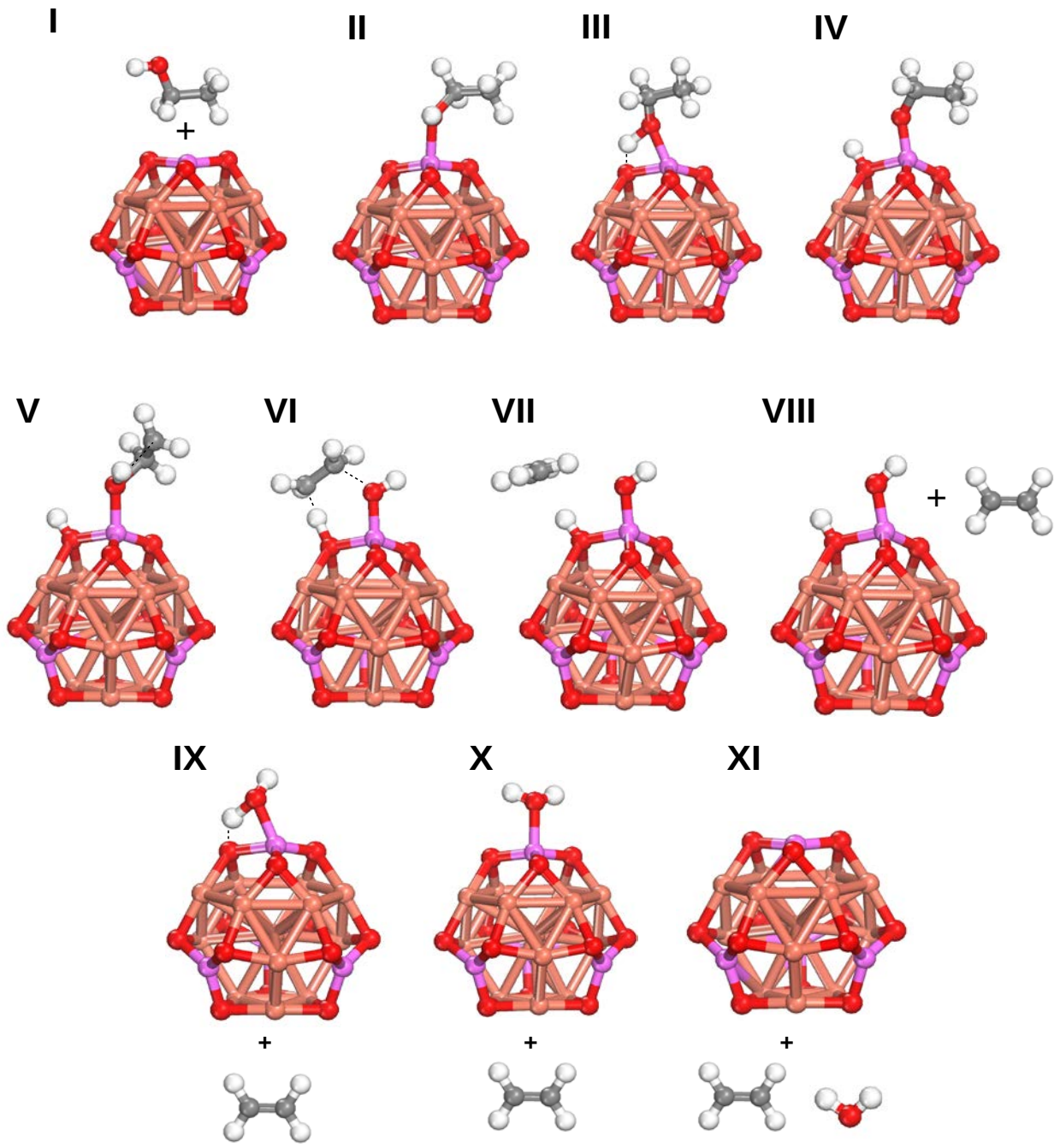


**Figure 16.** Graphical representations of elementary reaction steps reported in Figure 15 for the competing ethylene formation mechanisms, using the $Cu_{13}Al_4O_{12}$ nanocluster as an example. The roman numerals above each structure correspond to individual energetic states of reaction steps reported in Figure 15.

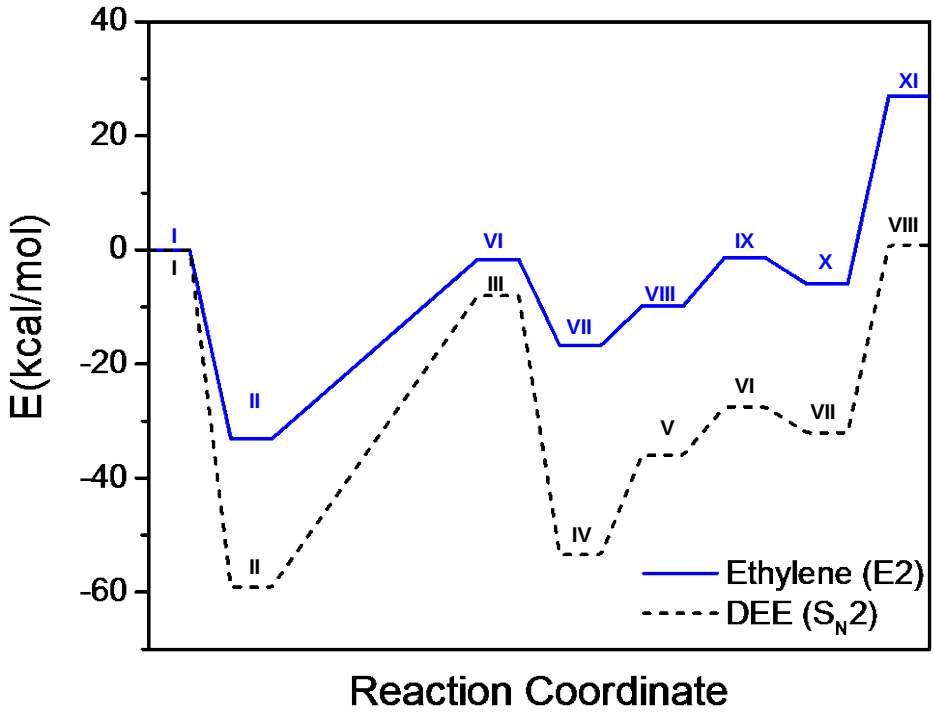


**Figure 17.** Reaction pathway energetics for DEE and ethylene formation on $Cu_{13}Al_4O_{12}$ via the $S_N2$ (black dashed line) and E2 mechanism (blue line), respectively. The roman numerals on each step of the DEE mechanism represent: I. reference state with the gas phase nanocatalyst and the two ethanol molecules in infinite separation, II. both ethanol molecules coadsorbed on the nanocluster (one chemisorbed and the other physisorbed), III. DEE formation TS, IV. physisorbed DEE and chemisorbed dissociated water on the nanocluster, V. DEE desorption, VI. water formation TS, VII. formation of adsorbed water, and VII. water desorption and regeneration of the nanocluster. The description of the roman numerals for ethylene formation (in blue) are the same as presented in the caption of Figure 15.

The olefin and the ether formation pathways are shown to be competing during ethanol dehydration.[29, 63] DEE formation has been shown to occur via the $S_N2$ mechanism, requiring co-adsorption of two alcohols on neighboring LA sites (see example of Al sites on $\gamma$-$Al_2O_3$ positioned at a distance of ~3.7 Å).[58] However, the distance between the Al centers on the nanoclusters in this study varies between 5.0-5.4 Å (as shown in Figure 13) due to the significant

curvature of the metal core. Consequently, the interaction of two ethanol molecules chemisorbed on Al sites to form DEE is not feasible. An alternative etherification route involves the chemisorption of one alcohol reacting with an additional physisorbed alcohol (Figure 17). The two interacting alcohols (one chemisorbed and one physisorbed as shown in structure II of Figure 18), react through a concerted transition state (III in Figure 18) in which DEE and a dissociated, surface-bound OH-H form in a single step (IV in Figure 18). Subsequent desorption of DEE and water complete the catalytic cycle. The detailed reaction energy profile for DEE formation is shown in Figure 17. Compared to the unimolecular (E2) pathway for olefin (i.e. ethylene) formation, olefin formation is energetically preferred ($E^a_{olefin}$ = 31.43 kcal/mol vs. $E^a_{ether}$ = 51.08 kcal/mol), highlighting the structure-based selectivity of these nanocatalysts. Since the etherification barrier on $Cu_{13}Al_4O_{12}$ was shown to be prohibitively high, the barriers were not calculated for the remaining nanoclusters. The E2 pathway for olefin formation on the same catalyst is also plotted in Figure 17 for comparison.

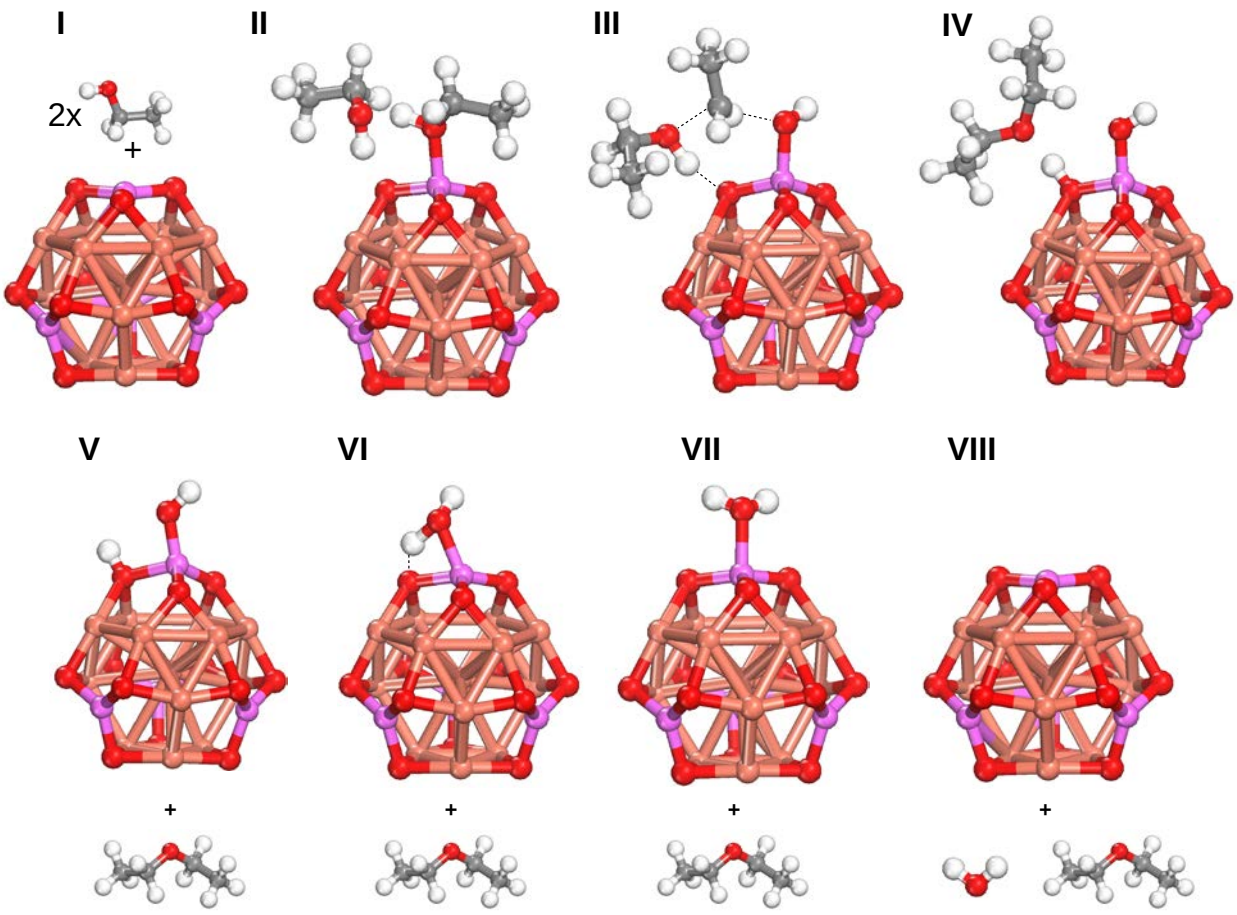


**Figure 18.** Graphical representations of elementary reaction steps reported in Figure 5 for the ether formation mechanism on the $Cu_{13}Al_4O_{12}$ nanocluster. The roman numerals above each structure correspond to individual energetic states of reaction steps reported in Figure 17.

## 5.4 CONCLUSIONS

Overall, the nanoscale engineering of these novel $M_{13}Al_4O_{12}$ nanocatalysts shown in this work is a unique example of *in-silico* rational catalyst design, utilizing composition and morphology (size/shape) of metal and metal-oxide systems to design stable and highly selective alcohol dehydration catalysts. This is made feasible by shutting down non-preferred (bimolecular)

reaction pathways through designing active sites on high-curvature nanoparticle surfaces. As a result, we report the first computational design of nanocatalysts that selectively convert ethanol to ethylene avoiding the DEE formation.

# 6.0 STRUCTURE-ACTIVITY RELATIONSHIPS ON $\gamma$-$Al_2O_3$: FROM ALCOHOL DEHYDRATION TO ALKANE DEHYDROGENATION

## 6.1 INTRODUCTION

Olefins are important chemical building blocks for the production of a wide range of valuable chemicals and plastics, with increasing demand worldwide. The low cost and high abundance of alkanes has motivated significant work in the field of olefin production via catalytic dehydrogenation. A number of catalysts have been evaluated for selective dehydrogenation of alkanes to form alkenes which can proceed through oxidative and nonoxidative dehydrogenation reactions. Metal oxides exhibiting acid-base surface functionalities have shown promise as non-oxidative dehydrogenation catalysts. Several oxide materials were shown to exhibit moderate to high catalytic activity, including $Al_2O_3$, $Ga_2O_3$, $Cr_2O_3$ and others[110-117]. Nakagawa et al. have shown that supported and unsupported $Ga_2O_3$ was active in alkane dehydrogenation, along with $Cr_2O_3$, $Fe_2O_3$, $Al_2O_3$ and $SiO_2$[115]. Although $Ga_2O_3$ has shown good dehydrogenation activity, a significant issue remains in catalyst deactivation. To combat catalyst deactivation, stable supports can be used to increase the stability of the metal oxide.

Group 5 and 6 transition metal oxides, typically supported on a stable oxide support have also shown promise as highly active, selective, and stable alkane dehydrogenation catalysts, finding industrial applications[111-112, 114-116, 118-123]. These catalyst systems are characterized by

presence of isolated surface sites that are active in catalyzing the dehydrogenation or alkanes. The CATOFIN process is based on chromium oxide catalyst supported on alumina[120], and is industrially used to produce propylene and isobutene from their corresponding alkanes. The complexity of the system has led to debate concerning the nature of surface active sites, with recent work pointing to isolated $Cr^{3+}$ surface species or small chromium oxide clusters, as the likely active sites[124-126]. The Lewis acid-base functionalities of metal oxides play a key role in their catalytic behavior. However, how these functionalities affect the alkane dehydrogenation behavior and how they can be rationalized on multisite surfaces of metal oxides, is still elusive.

Alkane dehydrogenation mechanisms on metal oxide active sites are debated in literature and vary with the type of catalysts and the nature of active sites present[127-129]. Although specific mechanisms are disputed, metal-alkyl complexes have been shown to be key intermediates in alkane dehydrogenation on several oxides[117, 124-126]. Activation takes place on metal (LA) centers on the oxide surface, forming organometallic intermediates (M-alkyl), which proceed to hydrogen elimination and olefin formation. Low coordination number, isolated metal centers exhibit high activity[117]. Aluminum oxide is known to exhibit strong acid-base properties, with recent work by Hargreaves et al.[113] showing $Al_2O_3$ to be active in H/D exchange reactions. The authors attributed the increased activity to inherent acidity and basicity of surface acid-base pairs, exhibiting highest quantities for undercoordinated surface sites.

Recent experimental work on alkane dehydrogenation by Rodemerck et al.[130] has shown aluminum oxide to be an active catalyst in dehydrogenation of propane, exhibiting good activity and selectivity towards the olefin product. The authors attributed the observed catalytic activity to presence of coordinatively unsaturated Lewis acid-base sites, generated at high temperatures by removal of surface hydroxyl groups which form in the presence of water[37, 94]. Surface

hydroxylation can poison the catalyst surface and is a commonly-observed phenomenon, studied extensively in recent experimental and computational studies[37, 94]. High-temperature pretreatment of the catalyst or extended time on stream at reaction conditions likely removes surface water, thus exposing the most active surface sites[37, 94, 131].

Joubert et al. investigated propane dehydrogenation activity of $Al_2O_3$ support in a supported catalyst systems and showed that dehydrogenation can occur at moderate activation barriers on the alumina support material[132-133]. The authors evaluated nonoxidative propane dehydrogenation via concerted and sequential pathways, with the former proceeding via dissociation of two C-H bonds in a single catalytic step.

Of the different thermodynamics phases of alumina, $\gamma$-$Al_2O_3$ has been shown to be an active catalyst and a stable support material for a range of catalytic applications and various chemistries [59-61, 66, 113, 129, 131]. The exact crystallographic structure of bulk alumina is not well defined, but it is known that $Al^{3+}$ cations are distributed within the bulk in tetrahedral and octahedral positions, exposing undercoordinated surface sites of Al-O Lewis acid-base pairs[37, 94]. Tricoordinated aluminum centers ($Al^{CN3}$) have been shown to exist on the (110) facets of $\gamma$-$Al_2O_3$[37, 61, 94, 131] and reported to exhibit the highest degree of Lewis acidity[61]. Cluster models of strongly acidic tricoordinated $Al^{3+}$ LA cites on $\gamma$-$Al_2O_3$ have been used as representative of the local coordination environment on alumina (110) facets. These models were used in several recent computational studies of alcohol dehydration chemistry[60, 66, 134]. Excellent agreement was observed between calculated activation energy barriers and those measured experimentally for alcohols of varying chain length and degree of substitution. In addition, dehydration activity SARs were constructed based on physicochemical descriptors of the catalyst and reacting alcohols, towards screening of oxide catalytic systems, based on fundamental properties.

Progress has been made in understanding the surface chemistry on oxides in terms of active sites and mechanisms, however debate still exists in both areas and significant research is still required. Further research on alkane dehydration on $\gamma$-$Al_2O_3$ can provide a more complete mechanistic understanding, adding to the current state of the art.

In this work we investigate nonoxidative dehydrogenation of several alkanes of varying size and degree of branching (ethane, propane, n-butane and i-butane) over an alumina cluster model of $\gamma$-$Al_2O_3$, which exposes undercoordinated $Al^{3+}$ acid centers using *ab-initio* electronic structure calculations. We examine two competing mechanisms on acid-base site pairs of the oxide surface, namely a sequential and a concerted pathway for the four hydrocarbons in question and show an energetic preference for the concerted pathway in all cases. Finally, using previously-reported methodology, we developed a dehydrogenation model, based on fundamental properties of the catalyst and reacting hydrocarbons as a potential screening tool for oxide catalysts.

## 6.2 COMPUTATIONAL METHODS

DFT calculations were performed to study $Al_2O_3$-catalyzed dehydrogenation of ethane, propane, n-butane and i-butane. Cluster models have been used extensively as model systems to investigate species adsorption and reactions on metal oxide surfaces and shown to accurately capture the physics of surface reactions[60, 135]. The model cluster used in this work (Figure 19) consists of 8 metal and 12 oxygen atoms and has been previously used to simulate alcohol dehydration active sites (tricoordinated LA sites) on alumina, in excellent agreement with experimental dehydration results [60]. All energy calculations were performed using the B3LYP[67-

[68] hybrid functional as implemented in Gaussian 09 package[70], with the 6-311G* triple-ζ basis set used for Al, O, C and H atoms. Reaction pathways were mapped by scanning the potential energy surface of the reaction coordinate. The energy maxima were fully relaxed to a saddle point to locate the actual transition states. In addition, we used the Synchronous Transit-Guided Quasi-Newton (STQN) method to locate relevant transition states. All transition states and local minima were obtained by full optimizations and verified by vibrational frequency and Intrinsic Reaction Coordinate (IRC) calculations [136]. The BE of reactants on the LA site of the metal oxide clusters was calculated according to Equation (15):

$$BE = E_{ads} - E_{cluster} - E_{react} \quad (15)$$

Where, $E_{ads}$ is the total electronic energy of an adsorbed alkane on the oxide cluster, and $E_{cluster}$ and $E_{react}$ are total electronic energies of the bare cluster and alkanes, respectively. PA was used to quantify strength of oxygen base sites and was calculated according to Equation (16).

$$PA = E_{cluster+H^+} - E_{cluster} \quad (16)$$

Where $E_{cluster+H^+}$ and $E_{cluster}$ are the energies of the protonated and bare (neutral) cluster, as the electronic energy of a proton is zero.

## 6.3 RESULTS AND DISCUSSION

### 6.3.1 Energetic Comparison of Mechanisms

Although theoretical and experimental studies have been performed to elucidate the reaction mechanism for nonoxidative alkane dehydrogenation[110], extensive debate remains regarding the surface mechanism. We begin by assessing dehydrogenation of ethane via two different mechanisms - a sequential and a concerted pathway on surface Lewis acid-base site pairs of the $Al_8O_{12}$ cluster model shown in Figure 19.

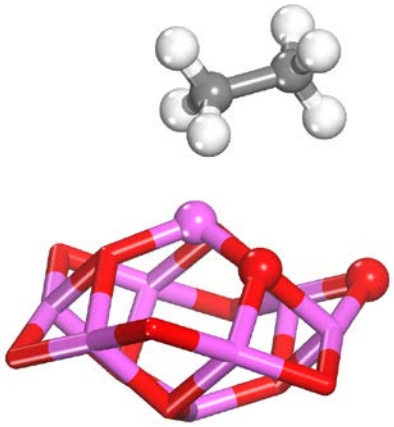

**Figure 19.** Ethane adsorption ground state on the $Al^{CN3}$ site of the $Al_8O_{12}$ cluster. Aluminum atoms are pictured in magenta, oxygen in red, carbon in grey and hydrogen in white.

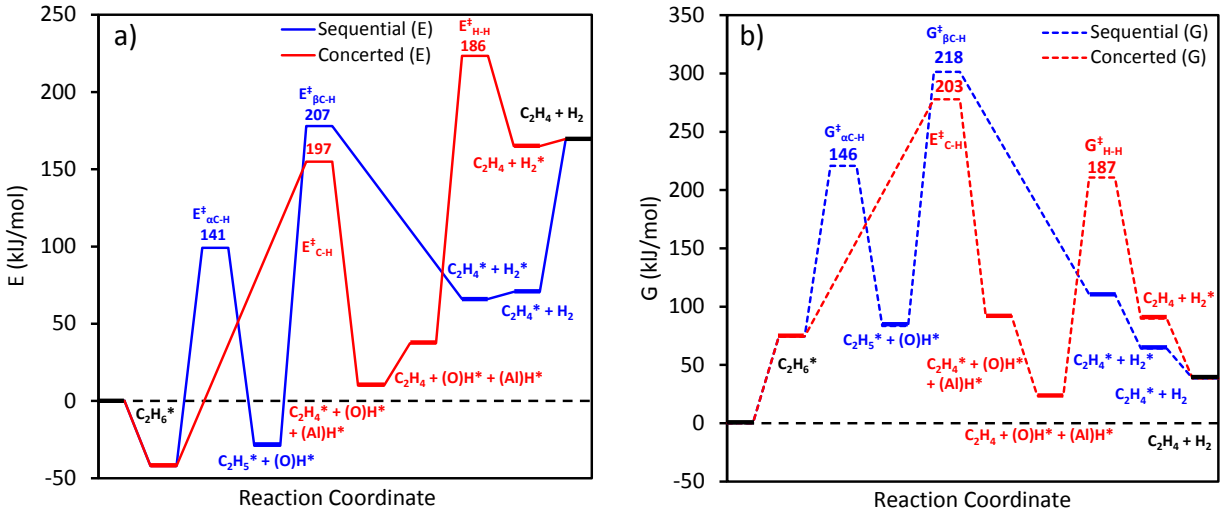


**Figure 20.** Energy profiles of ethane dehydrogenation via the concerted (red) and sequential (blue) pathways in terms of (a) Electronic energies – E and (b) Gibbs free energies – G. Energies of ground states and saddle points were referenced to reactants at infinite separation. Reaction barrier values for corresponding reaction steps are reported on the energy diagram. Values are reported in (kJ/mol), adsorbed states are denoted with asterisks (*) and transition states denoted with double daggers (‡).

Reaction energetics of the two mechanisms are reported in Figure 20, in terms of the electronic (E) and Gibbs free energies (G), referenced to gas-phase species at infinite separation. The free energies were calculated at a temperature of 823K, typical of experimental operating conditions. The first step in both mechanisms is adsorption of hydrocarbons on the active site of the catalyst and is shown to be a weak interaction that is weakly exothermic in terms of electronic energies and endothermic in terms of Gibbs free energies. The weak adsorption is characteristic of the high chemical stability of (saturated) alkanes that makes them difficult to process in catalytic applications.

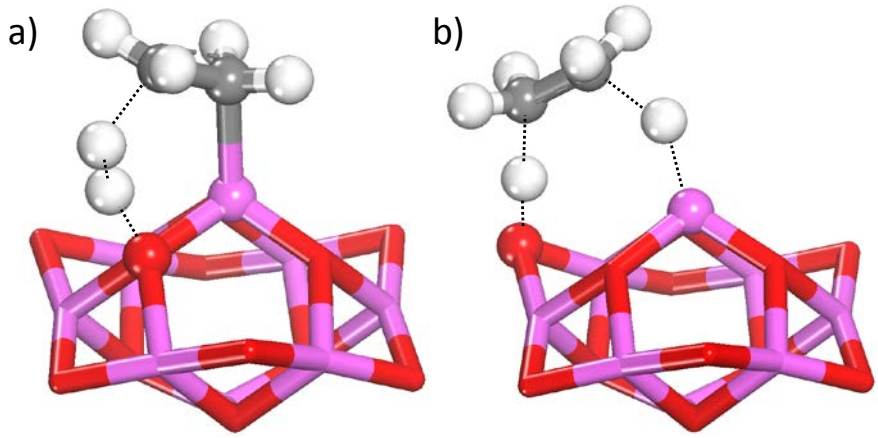


**Figure 21.** Graphical representation of transition states in beta-hydrogen elimination to form (a) molecular $H_2$ in the sequential pathway and (b) concerted hydrogen elimination to form ethylene and (dissociated) surface-bound hydrogen.

From the adsorbed state ($C_2H_6$*), the sequential mechanism (blue lines in Figure 20) is initiated by activation of a C-H bond (αC-H) and formation of an Al-bound organometallic complex with a neighboring O-H group ($C_2H_5$* + (O)H*) via heterolytic splitting. A number of alternative ground states were considered, including an alkoxide-like (O)$C_2H_5$* species bound on a neighboring oxygen base site, however the Al-bound $C_2H_5$ was found to be the most stable adsorption configuration. For the sequential pathway, the barrier for the initial C-H activation was found to be moderate, with calculated values of 141 kJ/mol and 146 kJ/mol in terms of electronic (E) and free energies (G), respectively. The next step in the sequential route was found to be the direct formation of molecular $H_2$ by elimination of the beta-hydrogen, featuring a 6-membered transition state (Figure 21a). The activation barrier ($E^{\ddagger}_{\beta C\text{-}H}$) for this step was shown to be rate-limiting, with calculated values of 207 kJ/mol and 218 kJ/mol, in terms of electronic and free energies, respectively. The catalytic cycle is completed by desorption of the weakly-bound

$H_2$ and ethylene adsorbates to regenerate the catalyst surface, with a net reaction endothermicity of 170 kJ/mol and 39 kJ/mol in terms of electronic and free energies, respectively.

In the concerted pathway (red lines in Figure 20) upon adsorption, the alkane molecule proceeds to dehydrogenate directly to the olefin product via simultaneous cleavage of two C-H bonds. The activation energy barriers ($E^{\ddagger}_{C\text{-}H}$) were found to be lower than those in the sequential pathway, with calculated electronic and free energy values of 197 kJ/mol and 203 kJ/mol, respectively. The concerted pathway features a 6-center transition state (Figure 21b) in which the surface LA center and a neighboring base site abstract the hydrogen atoms, resulting in formation of the alkene and a surface-bound hydrogen in the dissociated state. The catalytic cycle is completed by formation of molecular hydrogen via an associative transition state between the $Al^{CN3}$ and a peripheral oxygen base site, with calculated electronic and free energy barriers of 186 kJ/mol and 187 kJ/mol, respectively (Figure 20). It is important to note that this hydrogen formation barrier is quite high between the twofold coordinated peripheral oxygen site and the acid center, however it is plausible that a surface oxygen-bound proton can diffuse on the oxide surface to a threefold coordinated base site that is in closer proximity to the $Al^{CN3}$ center. The surface diffusion barrier was calculated to be 119 kJ/mol in terms of electronic energy. The corresponding hydrogen formation barriers between the neighboring acid-base pair decrease to 135 kJ/mol and 136 kJ/mol in terms of electronic and free energy barriers, respectively.

Based on the potential energy landscape shown in Figure 20, the rate-limiting elementary steps in the concerted pathway are favored relative to the sequential route by 15 kJ/mol in Gibbs free energy. The free energies reported in Figure 20 appear to reveal an entropic effect that further favors the concerted pathway, as evidenced by the exothermic (favored) desorption of alkene and $H_2$ products and comparable free energy barriers for all elementary steps. This energetic

favorability of the concerted pathway was confirmed for all of the hydrocarbons considered in this work, with the calculated reaction barriers reported in Table 1. In addition the relevant barriers for the sequential pathway were reported in Table 2, reporting barriers for the initial C-H activation (TS1) and the subsequent beta-hydrogen elimination (TS2), in terms of electronic and free energy barriers, respectively. It should be noted that the barriers reported in Table 1 correspond to reactions involving the more basic twofold coordinated oxygen site on the periphery of the cluster (see Figure 19). However, concerted dehydrogenation barriers corresponding to reactions between the neighboring threefold-coordinated oxygen center and $Al^{CN3}$ are increased (see Figure 22), likely due to the decreased basicity of the more coordinated $O^{CN3}$. Finally, it should be noted that the transition state for isobutane dehydrogenation via the concerted pathway could not be located in the case involving the $O^{CN3}$ site, after exhausting a number of available methods. It can potentially be rationalized by the bulky nature of the molecule and short interatomic distance of the $Al^{CN3}$-$O^{CN3}$ site pair. The calculated dehydrogenation reaction energetics for all four hydrocarbons via the sequential and concerted pathways are reported in Appendix A9.

**Table 1.** Calculated C-H activation barriers for the concerted pathway in terms of electronic (E) and free energies (G), reported in (kJ/mol).

| Species | $E_a$ (kJ/mol) | $G_a$ (kJ/mol) |
|---|---|---|
| Ethane | 197 | 203 |
| Propane | 169 | 170 |
| n-Butane | 169 | 168 |
| i-Butane | 148 | 156 |

**Table 2.** Calculated elementary step barriers for the sequential pathway in terms of electronic and free energies.

| Species | TS1-$E_a$ (kJ/mol) | TS1-$G_a$ (kJ/mol) | TS2-$E_a$ (kJ/mol) | TS2-$G_a$ (kJ/mol) |
|---|---|---|---|---|
| Ethane | 141 | 146 | 207 | 218 |
| Propane | 133 | 136 | 187 | 184 |
| n-Butane | 136 | 132 | 184 | 186 |
| i-Butane | 141 | 148 | 170 | 163 |

A clear effect of alkane substitution can be observed in terms of calculated barriers for the concerted pathway, with the barriers decreasing for more substituted species. The transition state in the concerted elimination pathway was found to have carbenium ion character for all hydrocarbons, with a calculated partial charges of +0.35, +0.61, +0.67 and +0.75 for ethane, propane, n-butane and i-butane, respectively. The increased partial charge of the more substituted species can be attributed to the presence of additional methyl (electron donating) substituents that stabilize the carbocation intermediate. The calculated partial charges in the transition state correlate with the calculated activation energies reported in Table 1 and are found to correlate linearly with CIS of the four hydrocarbons, as shown in Figure 22. CIS has been used as a physicochemical descriptor in alcohol dehydration chemistry which also involves formation of carbenium ions in the transition state[59, 66, 76].

### 6.3.2 Descriptor-Based Model Development

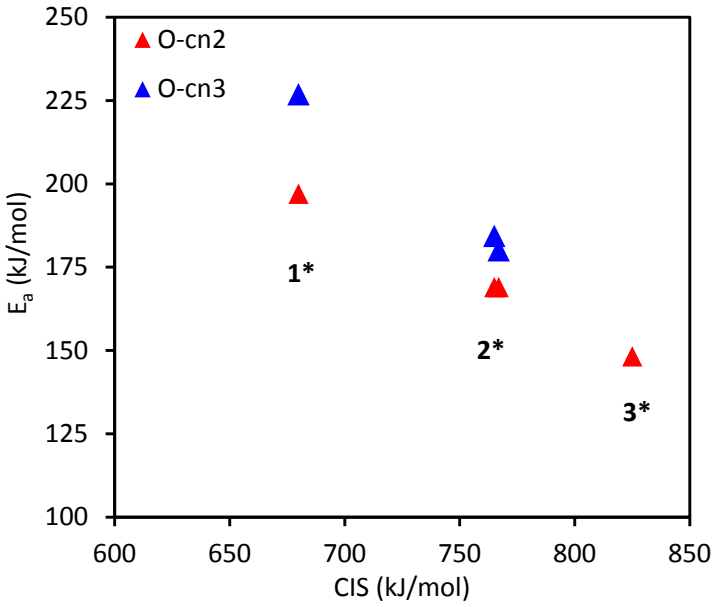


**Figure 22.** Calculated dehydrogenation (electronic) energy barriers for all alkanes involving the twofold- (red) and threefold- (blue) coordinated surface oxygen base sites plotted vs. CIS. Data points corresponding to primary, secondary and tertiary carbocation intermediates are denoted with corresponding numerical insets.

In addition to a physicochemical descriptor for reactant stability (CIS), suitable descriptors can be used to quantify Lewis acidity and basicity of the catalyst surface. Reactant BE and base site PA have been used as quantitative descriptors of surface acidity and basicity and applied in developing SARs for alcohol dehydration[59, 66]. Using a methodology previously used in dehydration of alcohols on LA clusters[59, 66], we developed a dehydrogenation model (Equation (17)) that applies the aforementioned descriptors in alkane dehydrogenation, by performing a multi-parameter linear regression of the calculated reaction barriers.

$$E_a = 620.3 - 0.39*CIS - 0.59*BE - 0.19*PA \quad (17)$$

Comparison of model-predicted and DFT-calculated activation energies of rate limiting step for the concerted pathway is shown in Figure 23, with good agreement observed between the two sets. The effect of CIS and base site PA on the calculated reaction barriers is captured for all reactants, with the largest deviation observed for ethane activation energies.

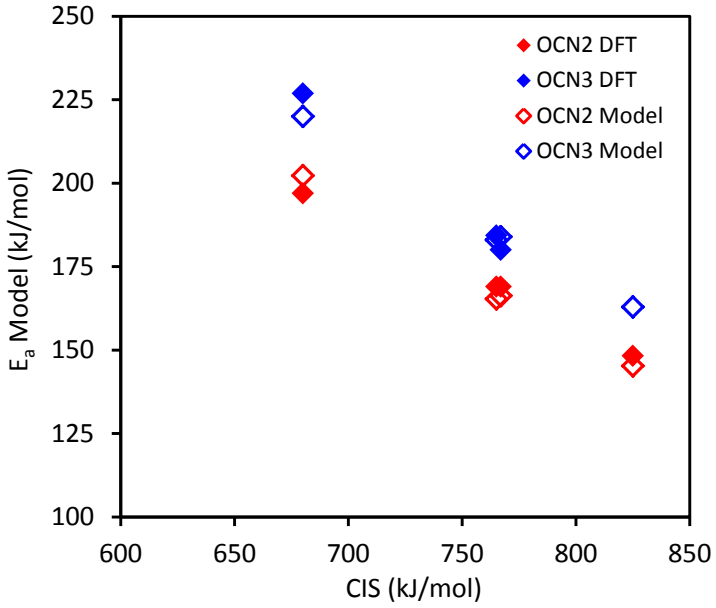


**Figure 23.** Calculated dehydrogenation (electronic) energy barriers for all alkanes involving the twofold- (red) and threefold- (blue) coordinated surface oxygen base sites plotted vs. CIS. Data points corresponding to primary, secondary and tertiary carbocation intermediates are denoted with corresponding numerical insets.

Interestingly, SARs developed for alcohol dehydration reactions on model clusters of metal oxide catalysts[59, 66] were able to capture the effect of reactant substitution (CIS) and catalyst acid-base properties (BE, PA) on model-predicted barrier values. This can be attributed to

structural similarity at the transition sate between alcohol dehydration and alkane dehydrogenation reactions, evolving through a concerted mechanism, shown in Appendix A10. A parity plot of DFT-calculated values versus SAR predictions of the dehydrogenation (red) and dehydration (blue) models is shown in Figure 24. The reaction barriers associated with alcohol dehydration are well-captured by the previously-developed[66] dehydration model, accounting for acid-base effects, and alcohol substitution. The fundamental difference between alcohol and alkane chemistry is captured by our descriptor-based models, where the strong binding of alcohols on LA sites of the oxides results in an anchoring effect – facilitating the dehydration to olefins. The high chemical stability of alkanes causes steeper reaction barriers, requiring higher energetic inputs (temperature) to catalyze the dehydrogenation, as reflected in experiments[59-60, 130].

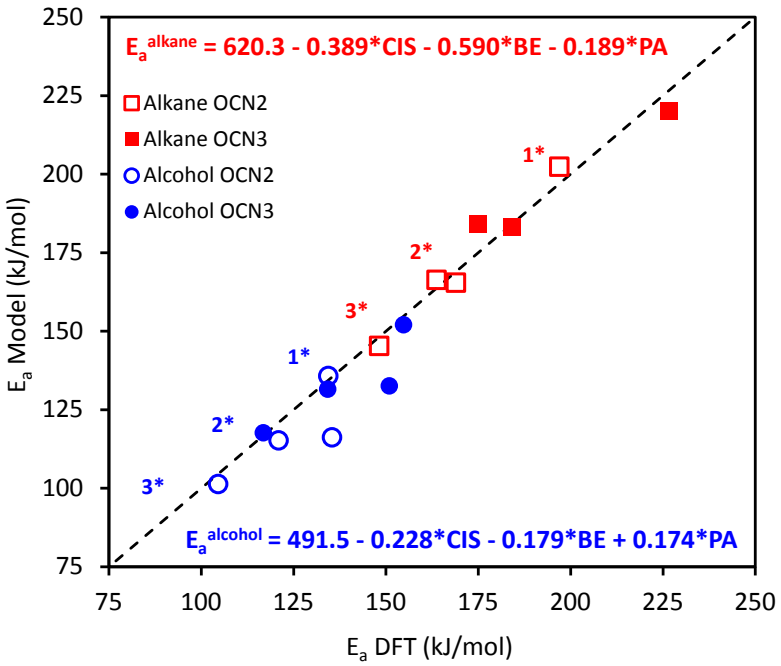


**Figure 24.** Parity plot of model-predicted and DFT-calculated reaction barriers for alkane dehydrogenation (red) and alcohol dehydration (blue). The calculated barriers are resolved by coordination of the catalytic (oxygen) base site and substitution of hydrocarbons involved in the reactions (open & filled symbols). Model equations for the dehydrogenation and dehydration SARs are shown as figure insets. Values are reported in (kJ/mol)

## 6.4 CONCLUSIONS

The dehydrogenation model developed in this work can be a useful screening tool in evaluating LA-catalyzed alkane systems for selective formation of olefins by nonoxidative dehydrogenation. The model accounts for fundamental system properties, quantified by descriptors of catalyst acidity (BE), basicity (PA) and reactant stability (CIS) in predicting the catalytic performance. Importantly, the same fundamental descriptors also apply to alcohol dehydration chemistry on metal oxides and, as shown in Figure 24, the SARs capture fundamental differences between alcohols and (the more stable) alkanes, as reflected by the

calculated barriers. The difference between alcohol and alkane chemistry lays in the anchoring effect on the catalyst surface via alcohol hydroxyl functionalities, in contrast to largely unreactive alkane molecules. This highlights the flexibility of this type of model as a tool in screening catalysts of large complexity by generalizing them based on shared physicochemical properties of the relevant active sites, towards a rational design of active and selective catalysts for the production of olefins and beyond.

# 7.0 FUTURE WORK

## 7.1 ALKANE DEHYDROGENATION STRUCTURE-ACTIVITY RELATIONSHIPS: BEYOND ALUMINA

Alkane dehydrogenation model summarized in Chapter 7 was applied in a predictive fashion towards the dehydrogenation activity of a gallium oxide catalyst. The linear model (parametrized for $Al_2O_3$) accounts for the reactant stability via CIS and catalyst acid-base properties via adsorbate BE and base site PA.

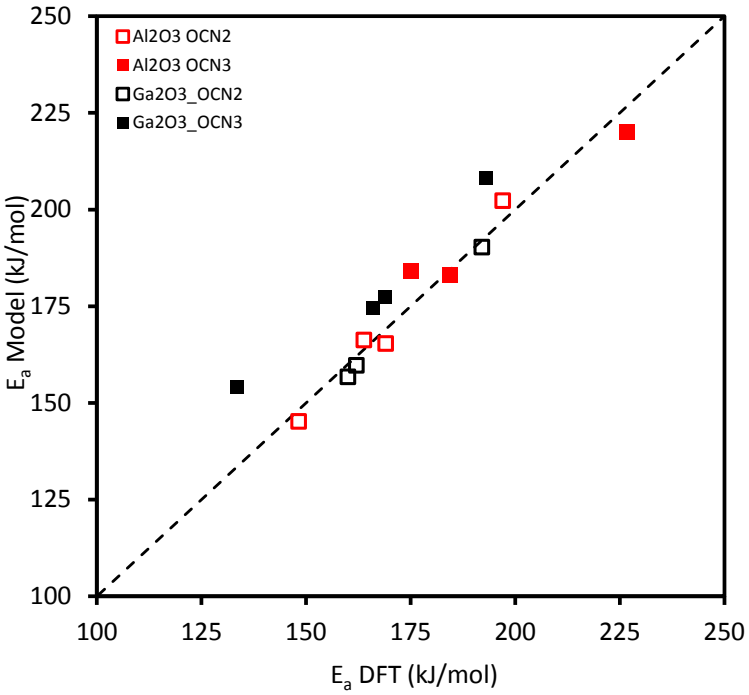


**Figure 25.** Parity plot of model-predicted and DFT-calculated reaction barriers for alkane dehydrogenation via $Al_2O_3$ (red) and $Ga_2O_3$ (black) catalytic systems.

The parity between model-predicted and DFT-calculated dehydrogenation barriers is reported in Figure 25 and shows that good agreement exists between the two. It is important to note that the current model was parametrized for the case of $Al_2O_3$, using 7 data points as the training set, yet the major trends in the case of gallium oxide are captured, as evidenced by the parity in Figure 25. In future work, the existing SARs can be extended to a greater number of oxide materials, towards screening of active alkane dehydrogenation catalysts. The accuracy of such models can be verified with additional DFT calculations, using the methodology applied in this work.

# APPENDIX A

# SUPPORTING INFORMATION

## A.1 REACTION ENERGETICS FOR ALCOHOL DEHYDRATION ON OXIDES

Energy diagrams of reaction pathways for the (ethyl) alcohol dehydration via intramolecular and E2 elimination mechanisms, on the metal oxides studied: Alox, Gaox, Inox, Ga-Alox and In-Alox. The dehydration of 1-propanol, 2-propanol and t-butanol (not shown) evolved through the same pathways. Adsorbed species are denoted with an asterisk (*). Transition states are denoted with a double dagger ($^{\ddagger}$).

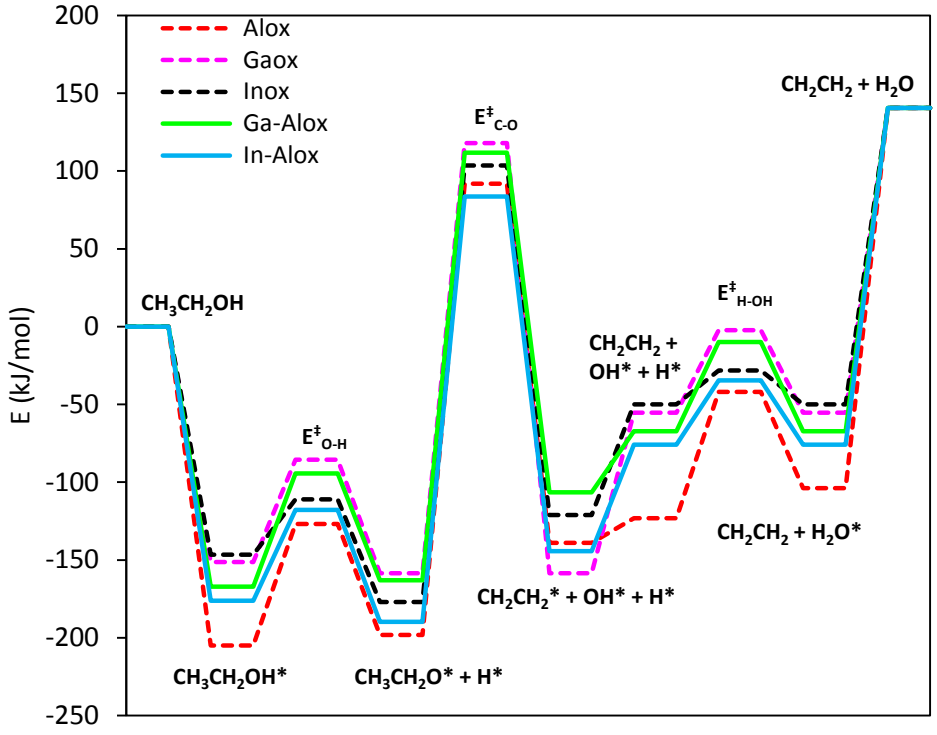


**Figure 26.** Ethanol dehydration reaction pathway energetics for the intramolecular mechanism on five metal oxide catalysts investigated in this work.

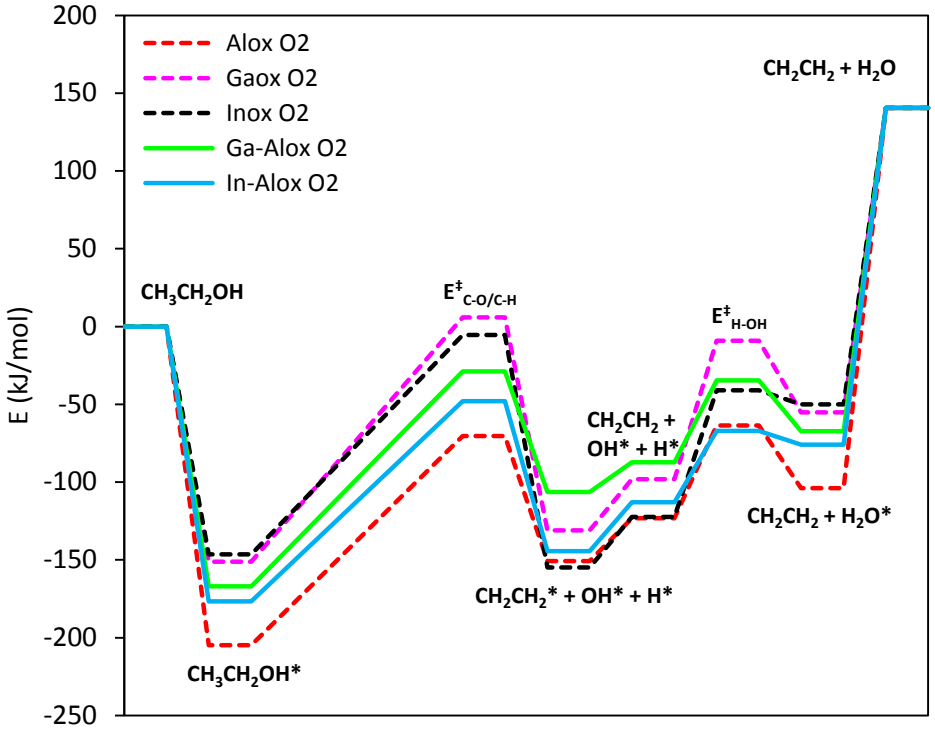


**Figure 27.** Ethanol dehydration reaction pathway for the E2 mechanism, involving twofold-coordinated ($O^{CN2}$) $H^{\beta}$ abstarctions site, on five metal oxide catalysts investigated in this work.

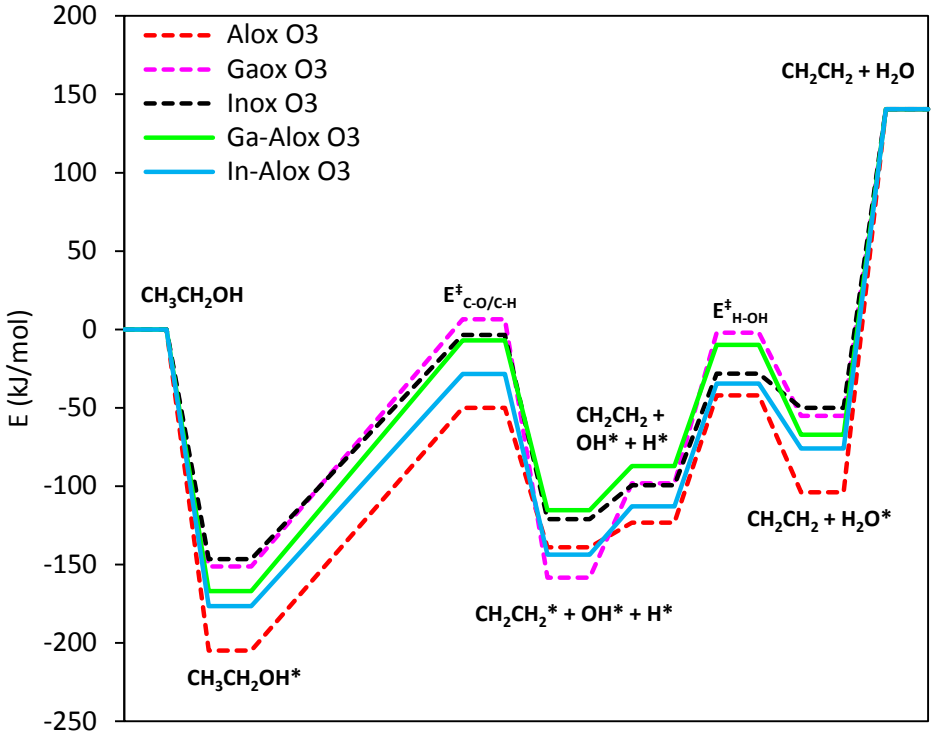


**Figure 28.** Ethanol dehydration reaction pathway for the E2 mechanism, involving threefold-coordinated ($O^{CN3}$) $H^{\beta}$ abstractions site, on five metal oxide catalysts investigated in this work.

## A.2 REACTION ENERGETICS FOR ETHER DECOMPOSITION ON OXIDES

Energy diagrams of reaction pathways for DEE decomposition via the E1-like and E2-like mechanisms, on five metal oxide clusters studied: Alox, Gaox, Inox, Ga-Alox and In-Alox. The decomposition of di-1-propyl ether, di-2-propyl ether and di-tert-butyl ether (not shown) evolved through the same pathways. Adsorbed species were denoted with an asterisk (*). Transition states were denoted with a double dagger ($^{\ddagger}$).

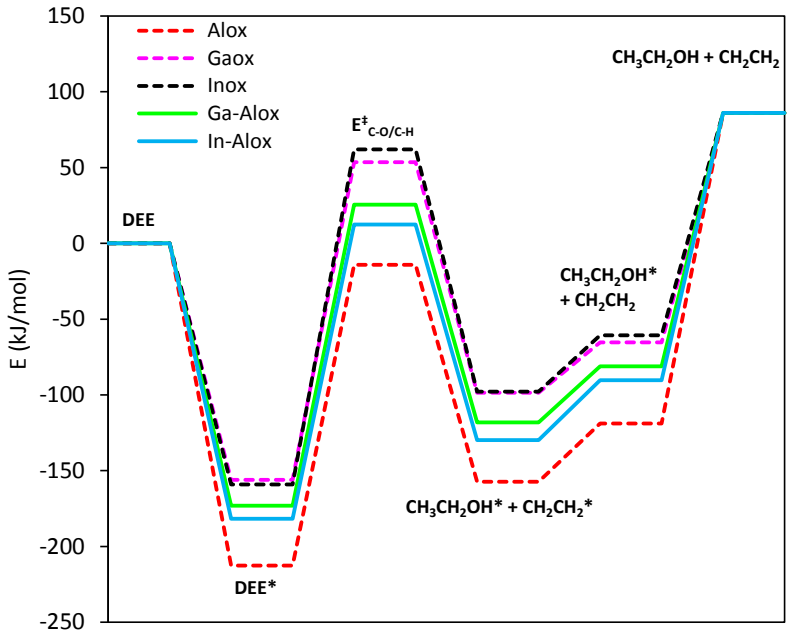


**Figure 29.** Diethyl ether decomposition reaction pathway for the E1-like mechanism on five metal oxide catalysts investigated in this work.

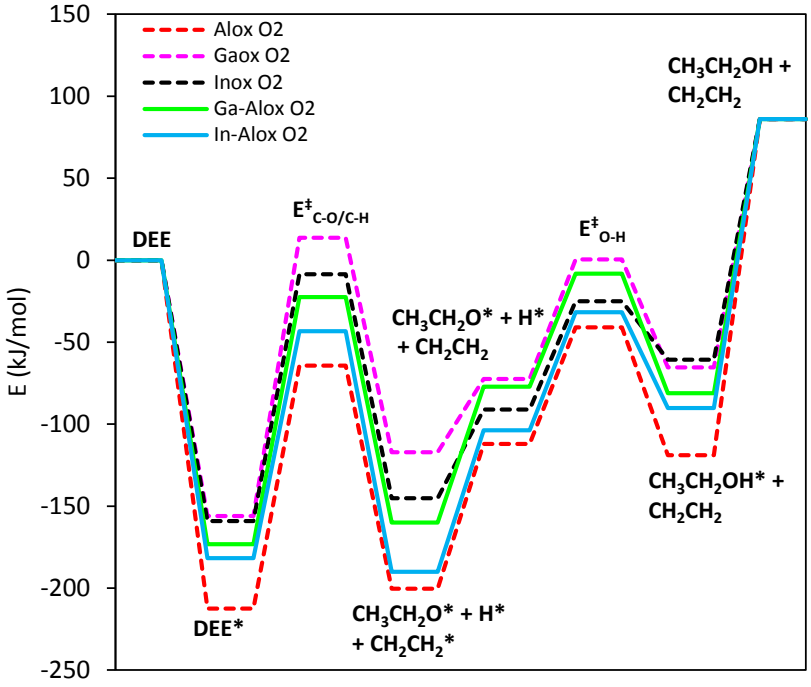


**Figure 30.** Diethyl ether decomposition reaction pathway for the E2-like mechanism, involving twofold-coordinated ($O^{CN2}$) H abstarctions site, on five metal oxide catalysts investigated in this work.

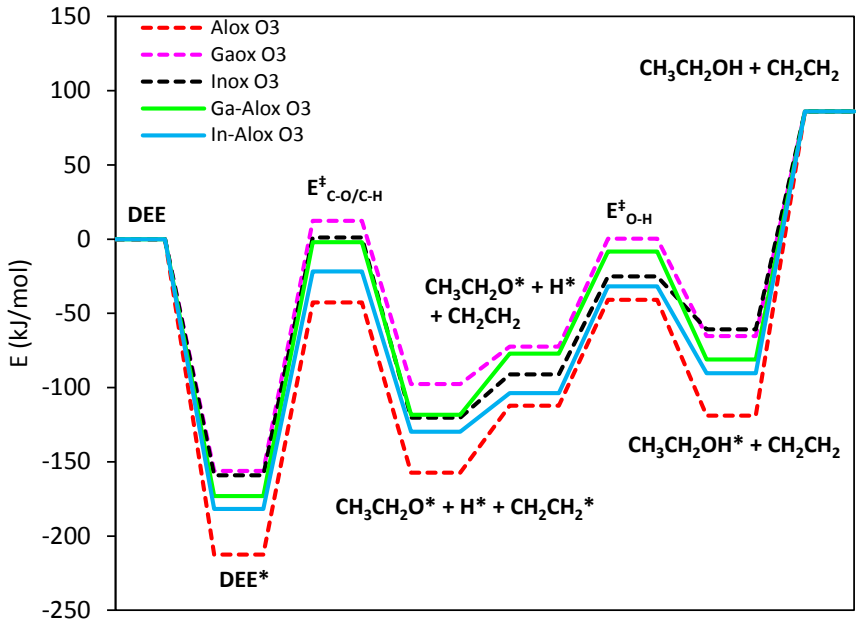


**Figure 31.** Diethyl ether decomposition reaction pathway for the E2-like mechanism, involving threefold-coordinated ($O^{CN3}$) H abstarctions site, on five metal oxide catalysts investigated in this work.

## A.3 ENERGETICS OF COMPETING MECHANISMS

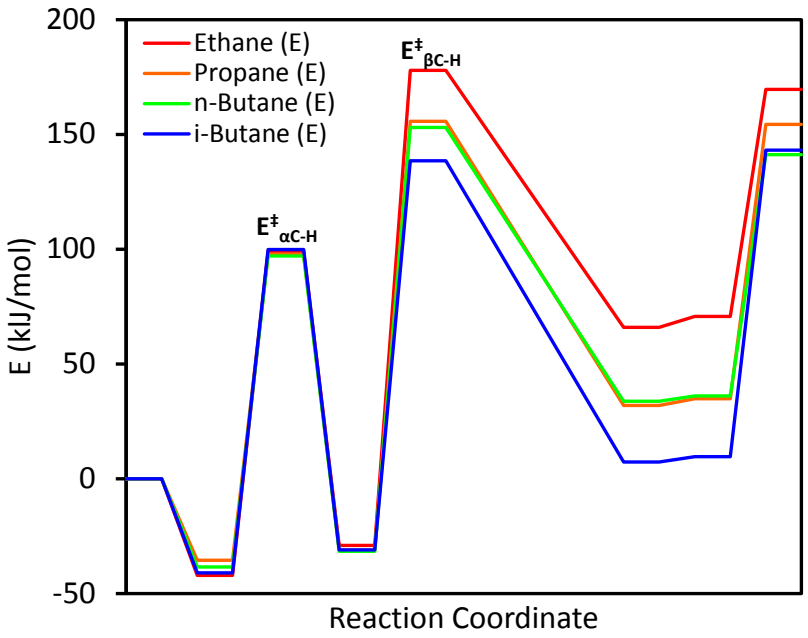


**Figure 32.** Energy profiles of alkane dehydrogenation via the sequential pathway in terms of Electronic energies – E. Energies of ground states and saddle points were referenced to reactants at infinite separation. Values are reported in (kJ/mol) and transition states are denoted with double dagger symbols (‡).

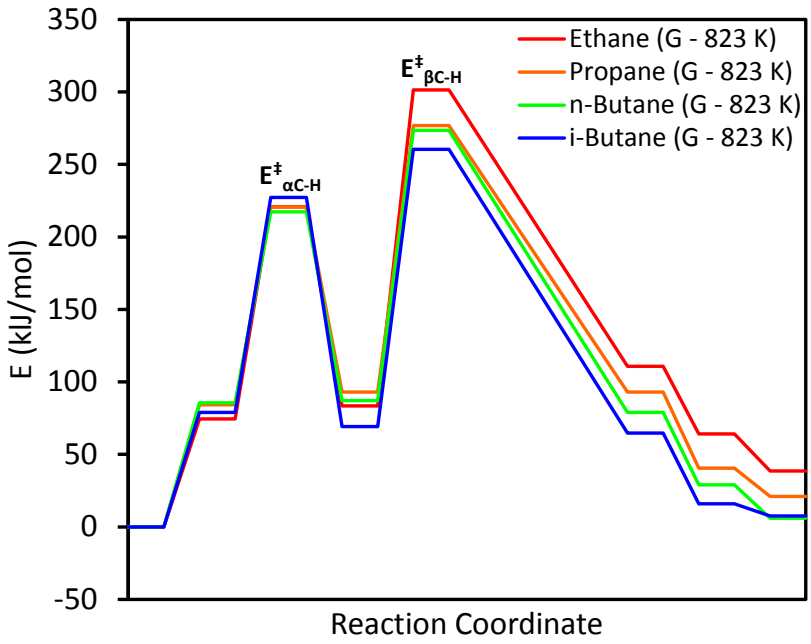


**Figure 33.** Energy profiles of alkane dehydrogenation via the sequential pathway in terms of Gibbs free energies – G, calculated at 823 K. Energies of ground states and saddle points were referenced to reactants at infinite separation. Values are reported in (kJ/mol) and transition states are denoted with double dagger symbols (‡).

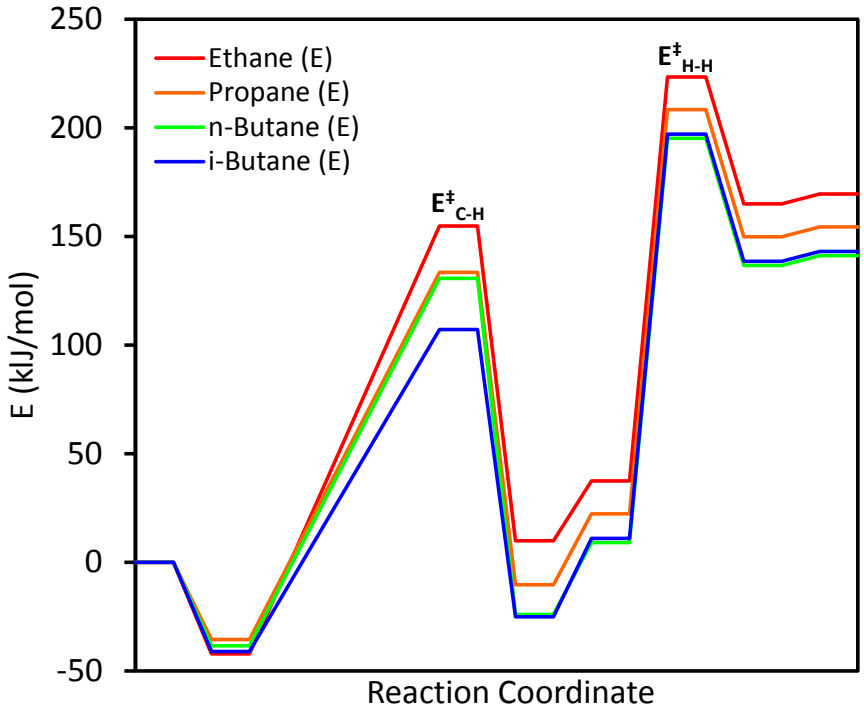


**Figure 34.** Energy profiles of alkane dehydrogenation via the concerted pathway in terms of Electronic energies – E. Energies of ground states and saddle points were referenced to reactants at infinite separation. Values are reported in (kJ/mol) and transition states are denoted with double dagger symbols (‡).

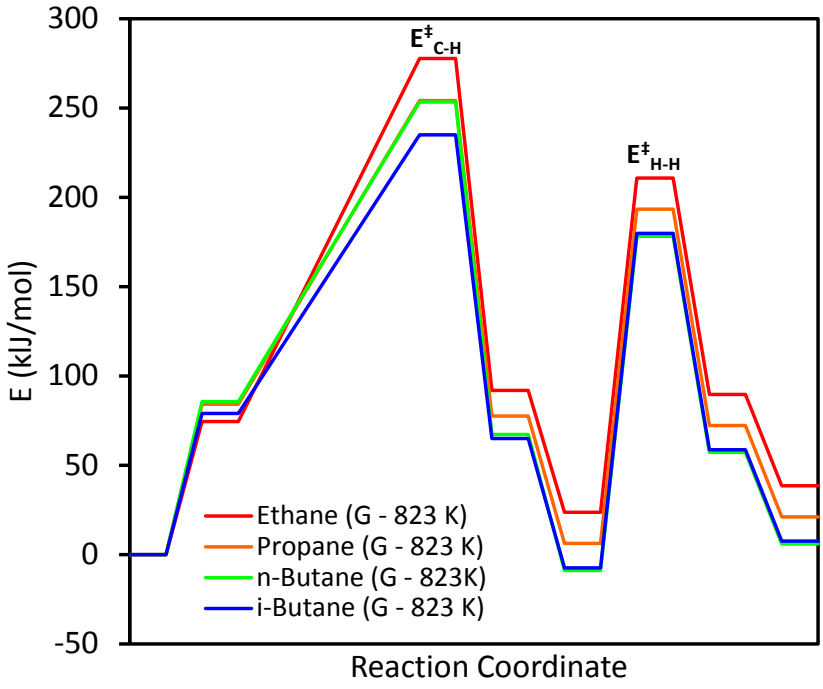


**Figure 35.** Energy profiles of alkane dehydrogenation via the concerted pathway in terms of Gibbs free energies – G, calculated at 823 K. Energies of ground states and saddle points were referenced to reactants at infinite separation. Values are reported in (kJ/mol) and transition states are denoted with double dagger symbols (‡).

## A.4 TRANSITION STATE COMPARISON

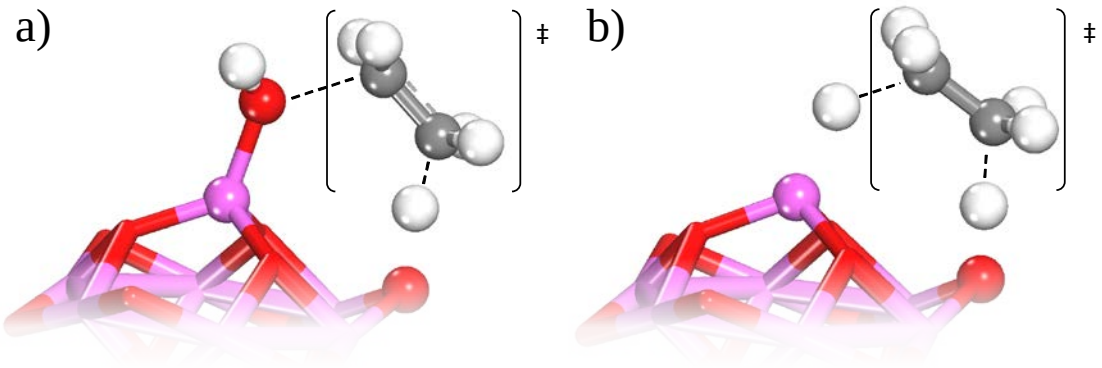


**Figure 36.** Graphical representations of concerted elimination transition states for a) alcohol (ethanol) dehydration and b) alkane (ethane) dehydrogenation, between acid (Al) and base (O) site pairs.

## BIBLIOGRAPHY


1. Huber, G. W.; Chheda, J. N.; Barrett, C. J.; Dumesic, J. A., Production of Liquid Alkanes by Aqueous-Phase Processing of Biomass-Derived Carbohydrates. *Science* **2005**, *308*, 1446-1450.

2. Huber, G. W.; Dumesic, J. A., An Overview of Aqueous-Phase Catalytic Processes for Production of Hydrogen and Alkanes in a Biorefinery. *Catal. Today* **2006**, *111*, 119-132.

3. Izhar, Q.; Fahimuddin, S., Analysis of Global Energy Consumption Patterns. *Journal of Environmental Research And Development* **2013**, *7*, 1761-1773.

4. Groombridge, B.; Jenkins, M. D., *World Atlas of Biodiversity: Earth's Living Resources in the 21st Century*; University of California Press, 2002, p 11.

5. Groombridge B., J. M. D., Global Biodiversity: Earth's Living Resources in the 21st Century. **2000**, Page 11.

6. Kunkes, E. L.; Simonetti, D. A.; West, R. M.; Serrano-Ruiz, J. C.; Gartner, C. A.; Dumesic, J. A., Catalytic Conversion of Biomass to Monofunctional Hydrocarbons and Targeted Liquid-Fuel Classes. *Science* **2008**, *322*, 417-421.

7. Brandt, A.; Grasvik, J.; Hallett, J. P.; Welton, T., Deconstruction of Lignocellulosic Biomass with Ionic Liquids. *Green Chem.* **2013**, *15*, 550-583.

8. Ragauskas, A. J., et al., The Path Forward for Biofuels and Biomaterials. *Science* **2006**, *311*, 484-489.

9. Xing, R.; Subrahmanyam, A. V.; Olcay, H.; Qi, W.; van Walsum, G. P.; Pendse, H.; Huber, G. W., Production of Jet and Diesel Fuel Range Alkanes from Waste Hemicellulose-Derived Aqueous Solutions. *Green Chem.* **2010**, *12*, 1933-1946.

10. Vlachos, D. G.; Caratzoulas, S., The Roles of Catalysis and Reaction Engineering in Overcoming the Energy and the Environment Crisis. *Chem. Eng. Sci.* **2010**, *65*, 18-29.

11. Parikka, M., Global Biomass Fuel Resources. *Biomass & Bioenergy* **2004**, *27*, 613-620.

12. Alonso, D. M.; Wettstein, S. G.; Dumesic, J. A., Bimetallic Catalysts for Upgrading of Biomass to Fuels and Chemicals. *Chem. Soc. Rev.* **2012**, *41*, 8075-8098.

13. Climent, M. J.; Corma, A.; Iborra, S., Conversion of Biomass Platform Molecules into Fuel Additives and Liquid Hydrocarbon Fuels. *Green Chem.* **2014**, *16*, 516-547.

14. Luterbacher, J. S.; Alonso, D. M.; Dumesic, J. A., Targeted Chemical Upgrading of Lignocellulosic Biomass to Platform Molecules. *Green Chem.* **2014**, *16*, 4816-4838.

15. Zheng, A. Q.; Zhao, Z. L.; Chang, S.; Huang, Z.; Zhao, K.; Wu, H. X.; Wang, X. B.; He, F.; Li, H. B., Maximum Synergistic Effect in the Coupling Conversion of Bio-Derived Furans and Methanol over Zsm-5 for Enhancing Aromatic Production. *Green Chem.* **2014**, *16*, 2580-2586.

16. Elliott, D. C.; Beckman, D.; Bridgwater, A. V.; Diebold, J. P.; Gevert, S. B.; Solantausta, Y., Developments in Direct Thermochemical Liquefaction of Biomass: 1983-1990. *Energy & Fuels* **1991**, *5*, 399-410.

17. Hu, J.; Yu, F.; Lu, Y., Application of Fischer–Tropsch Synthesis in Biomass to Liquid Conversion. *Catalysts* **2012**, *2*, 303-326.

18. Chen, N. Y.; Degnan, T. F.; Koenig, L. R., Liquid Fuel from Carbohydrates. *Chemtech* **1986**, *16*, 506-511.

19. Weisz, P. B.; Haag, W. O.; Rodewald, P. G., Catalytic Production of High-Grade Fuel (Gasoline) from Biomass Compounds by Shape-Selective Catalysis. *Science* **1979**, *206*, 57-58.

20. Katzen, R.; Tsao, G. T., A View of the History of Biochemical Engineering. *Advances in biochemical engineering/biotechnology* **2000**, *70*, 77-91.

21. Dapsens, P. Y.; Mondelli, C.; Perez-Ramirez, J., Biobased Chemicals from Conception toward Industrial Reality: Lessons Learned and to Be Learned. *ACS Catal.* **2012**, *2*, 1487-1499.

22. Guo, N.; Caratzoulas, S.; Doren, D. J.; Sandler, S. I.; Vlachos, D. G., A Perspective on the Modeling of Biomass Processing. *Energy Environ. Sci.* **2012**, *5*, 6703-6716.

23. Roman-Leshkov, Y.; Barrett, C. J.; Liu, Z. Y.; Dumesic, J. A., Production of Dimethylfuran for Liquid Fuels from Biomass-Derived Carbohydrates. *Nature* **2007**, *447*, 982-U5.

24. Roman-Leshkov, Y.; Chheda, J. N.; Dumesic, J. A., Phase Modifiers Promote Efficient Production of Hydroxymethylfurfural from Fructose. *Science* **2006**, *312*, 1933-1937.

25. Corma, A.; Huber, G. W.; Sauvanauda, L.; O'Connor, P., Biomass to Chemicals: Catalytic Conversion of Glycerol/Water Mixtures into Acrolein, Reaction Network. *J. Catal.* **2008**, *257*, 163-171.

26. Vollhardt, P. C.; Schore, N. E., *J. Org. Chem.*; W. H. Freeman, 2010; Vol. 6.

27. Gorte, R. J., What Do We Know About the Acidity of Solid Acids? *Catal. Lett.* **1999**, *62*, 1-13.

28. Nguyen, C. M.; Reyniers, M. F.; Marin, G. B., Theoretical Study of the Adsorption of the Butanol Isomers in H-ZSM-5. *J. Phys. Chem. C* **2011**, *115*, 8658-8669.

29. Knözinger, H.; Köhne, R., Catalytical Dehydration of Aliphatic Alcohols on Gamma - $Al_2O_3$. *Journal of Catalysis* **1964**, *3*, 559-560.

30. Knözinger, H., Dehydration of Alcohols on Aluminum Oxide. *Angew. Chem. Int. Ed* **1968**, *7*, 791-805.

31. Knözinger, H.; Bühl, H.; Kochloefl, K., The Dehydration of Alcohols on Alumina: Xiv. Reactivity and Mechanism. *J. Catal.* **1972**, *24*, 57-68.

32. Knozinger, H.; Ratnasamy, P., Catalytic Aluminas - Surface Models and Characterization of Surface Sites. *Cat. Rev. - Sci. Eng.* **1978**, *17*, 31-70.

33. Knözinger, H.; Scheglila, A., Dehydration of Alcohols on Alumina .12. Kinetic Isotope Effects in Olefin Formation from Butanols. *J. Catal.* **1970**, *17*, 252-263.

34. Davis, B. H.; Cook, S.; Naylor, R. W., Catalytic Conversion of Alcohols .8. Gallium Oxide as a Dehydration Catalyst. *J. Org. Chem.* **1979**, *44*, 2142-2145.

35. Davis, B. H., Catalytic Conversion of Alcohols .6. Selectivity of Indium Oxide. *J. Catal.* **1978**, *52*, 435-444.

36. Knözinger, H.; Köhne, R., Dehydration of Alcohols over Alumina 1. Reaction Scheme. *J. Catal.* **1966**, *5*, 264-270.

37. Digne, M.; Sautet, P.; Raybaud, P.; Euzen, P.; Toulhoat, H., Hydroxyl Groups on Gamma-Alumina Surfaces: A Dft Study. *J. Catal.* **2002**, *211*, 1-5.

38. Digne, M.; Sautet, P.; Raybaud, P.; Toulhoat, H.; Artacho, E., Structure and Stability of Aluminum Hydroxides: A Theoretical Study. *J. Phys. Chem. B* **2002**, *106*, 5155-5162.

39. Lousada, C. M.; Johansson, A. J.; Brinck, T.; Jonsson, M., Reactivity of Metal Oxide Clusters with Hydrogen Peroxide and Water - a Dft Study Evaluating the Performance of Different Exchange-Correlation Functionals. *Phys. Chem. Chem. Phys.* **2013**, *15*, 5539-5552.

40. Piskorz, W.; Grybos, J.; Zasada, F.; Cristol, S.; Paul, J.-F.; Adamski, A.; Sojka, Z., Periodic Dft and Atomistic Thermodynamic Modeling of the Surface Hydration Equilibria and Morphology of Monoclinic $ZrO_2$ Nanocrystals. *J. Phys. Chem. C* **2011**, *115*, 24274-24286.

41. Piskorz, W.; Grybos, J.; Zasada, F.; Zapala, P.; Cristol, S.; Paul, J.-F.; Sojka, Z., Periodic Dft Study of the Tetragonal $ZrO_2$ Nanocrystals: Equilibrium Morphology Modeling and Atomistic Surface Hydration Thermodynamics. *J. Phys. Chem. C* **2012**, *116*, 19307-19320.

42. Yuan, P.-Q.; Ren, C.; Tan, X.-C.; Zhu, C.-C.; Cheng, Z.-M.; Yuan, W.-K., Acid Properties of $Wo_x$/T-$ZrO_2$ under Hydrothermal Environments: A Periodic Dft Study. *Comput. Theor. Chem.* **2012**, *991*, 150-153.

43. Mukhopadhyay, A. B.; Musgrave, C. B.; Sanz, J. F., Atomic Layer Deposition of Hafnium Oxide from Hafnium Chloride and Water. *J. Am. Chem. Soc* **2008**, *130*, 11996-12006.

44. Mukhopadhyay, A. B.; Sanz, J. F.; Musgrave, C. B., First-Principles Investigation of Hydroxylated Monoclinic $HfO_2$ Surfaces. *Chem. Mater.* **2006**, *18*, 3397-3403.

45. Nakajima, K.; Noma, R.; Kitano, M.; Hara, M., Titania as an Early Transition Metal Oxide with a High Density of Lewis Acid Sites Workable in Water. *J. Phys. Chem. C* **2013**, *117*, 16028-16033.

46. Chia, M.; Dumesic, J. A., Liquid-Phase Catalytic Transfer Hydrogenation and Cyclization of Levulinic Acid and Its Esters to Gamma-Valerolactone over Metal Oxide Catalysts. *Chem. Comm.* **2011**, *47*, 12233-12235.

47. Auroux, A.; Artizzu, P.; Ferino, I.; Solinas, V.; Leofanti, G.; Padovan, M.; Messina, G.; Mansani, R., Dehydration of 4-Methylpentan-2-Ol over Zirconia Catalysts. *Journal of the Chemical Society-Faraday Transactions* **1995**, *91*, 3263-3267.

48. Vittadini, A.; Selloni, A.; Rotzinger, F. P.; Gratzel, M., Structure and Energetics of Water Adsorbed at Tio2 Anatase (101) and (001) Surfaces. *Phys. Rev. Lett.* **1998**, *81*, 2954-2957.

49. Bahruji, H.; Bowker, M.; Brookes, C.; Davies, P. R.; Wawata, I., The Adsorption and Reaction of Alcohols on $TiO_2$ and $Pd/TiO_2$ Catalysts. *Appl. Catal. A.* **2013**, *454*, 66-73.

50. Lusvardi, V. S.; Barteau, M. A.; Farneth, W. E., The Effects of Bulk Titania Crystal-Structure on the Adsorption and Reaction of Aliphatic-Alcohols. *J. Catal.* **1995**, *153*, 41-53.

51. Rekoske, J. E.; Barteau, M. A., Kinetics and Selectivity of 2-Propanol Conversion on Oxidized Anatase $TiO_2$. *J. Catal.* **1997**, *165*, 57-72.

52. Vimont, A.; Lavalley, J. C.; Sahibed-Dine, A.; Arean, C. O.; Delgado, M. R.; Daturi, M., Infrared Spectroscopic Study on the Surface Properties of Gamma-Gallium Oxide as Compared to Those of Gamma-Alumina. *J. Phys. Chem. B* **2005**, *109*, 9656-9664.

53. Umegaki, T.; Kuratani, K.; Yamada, Y.; Ueda, A.; Kuriyama, N.; Kobayashi, T.; Xu, Q., Hydrogen Production Via Steam Reforming of Ethyl Alcohol over Nano-Structured Indium Oxide Catalysts. *J. Power Sources* **2008**, *179*, 566-570.

54. Ye, J. Y.; Liu, C. J.; Mei, D. H.; Ge, Q. F., Active Oxygen Vacancy Site for Methanol Synthesis from Co2 Hydrogenation on $In_2O_3$(110): A Dft Study. *ACS Catal.* **2013**, *3*, 1296-1306.

55. Branda, M. M.; Collins, S. E.; Castellani, N. J.; Baltanas, M. A.; Bonivardi, A. L., Methanol Adsorption on the Beta-$Ga_2O_3$ Surface with Oxygen Vacancies: Theoretical and Experimental Approach. *J. Phys. Chem. B* **2006**, *110*, 11847-11853.

56. Branda, M. M.; Garda, G. R.; Rodriguez, H. A.; Castellani, N. J., Methanol Decomposition on the Beta-$Ga_2O_3$(100) Surface: A Dft Approach. *Surf. Sci.* **2007**, *254*, 120-124.

57. Lavalley, J. C.; Daturi, M.; Montouillout, V.; Clet, G.; Arean, C. O.; Delgado, M. R.; Sahibed-dine, A., Unexpected Similarities between the Surface Chemistry of Cubic and Hexagonal Gallia Polymorphs. *Phys. Chem. Chem. Phys.* **2003**, *5*, 1301-1305.

58. Christiansen, M. A.; Mpourmpakis, G.; Vlachos, D. G., Density Functional Theory-Computed Mechanisms of Ethylene and Diethyl Ether Formation from Ethanol on Gamma-$Al_2O_3$(100). *ACS Catal.* **2013**, *3*, 1965-1975.

59. Kostestkyy, P.; Yu, J.; Gorte, R. J.; Mpourmpakis, G., Structure-Activity Relationships on Metal-Oxides: Alcohol Dehydration *Catal. Sci. Technol.* **2014**, *4*, 3861-3869.

60. Roy, S.; Mpourmpakis, G.; Hong, D.-Y.; Vlachos, D. G.; Bhan, A.; Gorte, R. J., Mechanistic Study of Alcohol Dehydration on Gamma-$Al_2O_3$. *ACS Catal.* **2012**, *2*, 1846-1853.

61. Jenness, G. R.; Christiansen, M. A.; Caratzoulas, S.; Vlachos, D. G.; Gorte, R. J., Site-Dependent Lewis Acidity of Gamma-$Al_2O_3$ and Its Impact on Ethanol Dehydration and Etherification. *J. Phys. Chem. C* **2014**, *118*, 12899-12907.

62. DeWilde, J. F.; Chiang, H.; Hickman, D. A.; Ho, C. R.; Bhan, A., Kinetics and Mechanism of Ethanol Dehydration on $\gamma$-$Al_2O_3$: The Critical Role of Dimer Inhibition. *ACS Catal.* **2013**, *3*, 798-807.

63. DeWilde, J. F.; Czopinski, C. J.; Bhan, A., Ethanol Dehydration and Dehydrogenation on Gamma-Al2o3: Mechanism of Acetaldehyde Formation. *ACS Catal.* **2014**, *4*, 4425-4433.

64. Kang, M. J.; DeWilde, J. F.; Bhan, A., Kinetics and Mechanism of Alcohol Dehydration on Gamma-$Al_2O_3$: Effects of Carbon Chain Length and Substitution. *ACS Catal.* **2015**, *5*, 602-612.

65. Knozinger, H.; Kohne, R., Catalytical Dehydration of Aliphatic Alcohols on Gamma -$Al_2O_3$. *J. Catal.* **1964**, *3*, 559-560.

66. Kostetskyy, P.; Mpourmpakis, G., Structure-Activity Relationships in the Production of Olefins from Alcohols and Ethers: A First-Principles Theoretical Study. *Catal. Sci. Technol.* **2015**, *5*, 4547-4555.

67. Becke, A. D., Density-Functional Thermochemistry .3. The Role of Exact Exchange. *J. Chem. Phys.* **1993**, *98*, 5648-5652.

68. Lee, C. T.; Yang, W. T.; Parr, R. G., Development of the Colle-Salvetti Correlation-Energy Formula into a Functional of the Electron-Density. *Phys. Rev. B* **1988**, *37*, 785-789.

69. Zhao, Y.; Truhlar, D. G., The M06 Suite of Density Functionals for Main Group Thermochemistry, Thermochemical Kinetics, Noncovalent Interactions, Excited States, and Transition Elements: Two New Functionals and Systematic Testing of Four M06-Class Functionals and 12 Other Functionals. *Theor. Chem. Acc.* **2008**, *120*, 215-241.

70. Frisch, M. J., et al., Gaussian, Inc., Wallingford Ct. **2010**.

71. Lukinskas, P.; Farcasiu, D., Theoretical Study of Hydrogen Dissociation on Dialuminum Oxide Clusters and Aluminum-Silicon-Oxygen Clusters, as Models of Extraframework Aluminum Species and Zeolite Lattice. *Appl. Catal. A.* **2001**, *209*, 193-205.

72. Maresca, O.; Allouche, A.; Aycard, J. P.; Rajzmann, M.; Clemendot, S.; Hutschka, F., Quantum Study of the Active Sites of the Gamma-Alumina Surface: Chemisorption and Adsorption of Water, Hydrogen Sulfide and Carbon Monoxide on Aluminum and Oxygen Sites. *Comput. Theor. Chem.* **2000**, *505*, 81-94.

73. Roy, S.; Mpourmpakis, G.; Hong, D. Y.; Vlachos, D. G.; Bhan, A.; Gorte, R. J., Mechanistic Study of Alcohol Dehydration on Gamma-$Al_2O_3$. *ACS Catal.* **2012**, *2*, 1846-1853.

74. vanSanten, R. A., The Cluster Approach to Molecular Heterogeneous Catalysis. *J. Mol. Catal. Chem.* **1997**, *115*, 405-419.

75. Hay, P. J.; Wadt, W. R., Abinitio Effective Core Potentials for Molecular Calculations - Potentials for K to Au Including the Outermost Core Orbitals. *J. Chem. Phys.* **1985**, *82*, 299-310.

76. Kostestkyy, P.; Maheswari, J. P.; Mpourmpakis, G., Understanding the Importance of Carbenium Ions in the Conversion of Biomass-Derived Alcohols with First-Principles Calculations. *J. Phys. Chem. C* **2015**, *119*, 16139-16147.

77. Kostetskyy, P.; Zervoudis, N. A.; Mpourmpakis, G., Carboranes: The Strongest Bronsted Acids in Alcohol Dehydration. *Catal. Sci. Technol.* **2017**, *7*, 2001-2011.

78. Gold, V.; Loening, K. L.; McNaught, A. D.; Sehmi, P., *Compendium of Chemical Terminology Iupac International Union of Pure and Applied Chemistry Recommendations*, 1987, p VIII+456P.

79. Boronat, M.; Corma, A., Are Carbenium and Carbonium Ions Reaction Intermediates in Zeolite-Catalyzed Reactions? *Appl. Catal. A.* **2008**, *336*, 2-10.

80. March, J.; Smith, M. B., *March's Advanced Organic Chemistry*; JOHN WILEY & SONS, 2007; Vol. ISBN 0-471-85472-7.

81. Pauling, L., Citation Classic - the Nature of the Chemical-Bond and the Structure of Molecules and Crystals - an Introduction to Modern Structural Chemistry. *Current Contents/Engineering Technology & Applied Sciences* **1985**, 16-16.

82. McMurry, J., *Organic Chemistry: A Biological Approach*; Thompson Brooks/Cole, 2007.

83. Janik, M. J.; Macht, J.; Iglesia, E.; Neurock, M., Correlating Acid Properties and Catalytic Function: A First-Principles Analysis of Alcohol Dehydration Pathways on Polyoxometalates. *J. Phys. Chem. C* **2009**, *113*, 1872-1885.

84. Feng, S.; Bagia, C.; Mpourmpakis, G., Determination of Proton Affinities and Acidity Constants of Sugars. *J. Phys. Chem. A* **2013**, *117*, 5211-5219.

85. Montgomery, J. A. F., M. J.; Ochterski, J. W.; Petersson, G. Alfonso, D., A Complete Basis Set Model Chemistry. Vi. Use of Density Functional Geometries and Frequencies. *J. Chem. Phys, 1999, 110 (6),2822−2827.*

86. Curtiss, L. A.; Redfern, P. C.; Raghavachari, K., Gaussian-4 Theory. *J. Chem. Phys.* **2007**, *126*, 12.

87. Hratchian, H. P.; Schlegel, H. B., Accurate Reaction Paths Using a Hessian Based Predictor-Corrector Integrator. *J. Chem. Phys.* **2004**, *120*, 9918-9924.

88. Kostestkyy, P.; Mpourmpakis, G.; Zervoudis, N. A., Carboranes: The Strongest Brønsted Acids in Alcohol Dehydration. *Catal. Sci. Technol.* **2017**, *7*, 2001-2011.

89. Alonso, D. M.; Bond, J. Q.; Dumesic, J. A., Catalytic Conversion of Biomass to Biofuels. *Green Chem.* **2010**, *12*, 1493-1513.

90. Chheda, J. N.; Huber, G. W.; Dumesic, J. A., Liquid-Phase Catalytic Processing of Biomass-Derived Oxygenated Hydrocarbons to Fuels and Chemicals. *Angew. Chem. Int. Ed.* **2007**, *46*, 7164-7183.

91. Stocker, M., Biofuels and Biomass-to-Liquid Fuels in the Biorefinery: Catalytic Conversion of Lignocellulosic Biomass Using Porous Materials. *Angew. Chem. Int. Ed.* **2008**, *47*, 9200-9211.

92. Macht, J.; Janik, M. J.; Neurock, M.; Iglesia, E., Mechanistic Consequences of Composition in Acid Catalysis by Polyoxometalate Keggin Clusters. *J. Am. Chem. Soc.* **2008**, *130*, 10369-10379.

93. DeWilde, J. F.; Chiang, H.; Hickman, D. A.; Ho, C. R.; Bhan, A., Kinetics and Mechanism of Ethanol Dehydration on Gamma-Al2o3: The Critical Role of Dimer Inhibition. *ACS Catal.* **2013**, *3*, 798-807.

94. Digne, M.; Sautet, P.; Raybaud, P.; Euzen, P.; Toulhoat, H., Use of Dft to Achieve a Rational Understanding of Acid-Basic Properties of Gamma-Alumina Surfaces. *Journ Catal.* **2004**, *226*, 54-68.

95. Larmier, K.; Chizallet, C.; Cadran, N.; Maury, S.; Abboud, J.; Lamic-Humblot, A.-F.; Marceau, E.; Lauron-Pernot, H., Mechanistic Investigation of Isopropanol Conversion on Alumina Catalysts: Location of Active Sites for Alkene/Ether Production. *ACS Catal.* **2015**, *5*, 4423-4437.

96. Eck, S.; Castellarin-Cudia, C.; Surnev, S.; Prince, K. C.; Ramsey, M. G.; Netzer, F. P., Adsorption and Reaction of Co on a Ceria-Rh(111) "Inverse Model Catalyst" Surface. *Surf. Sci.* **2003**, *536*, 166-176.

97. Rodriguez, J. A.; Hrbek, J., Inverse Oxide/Metal Catalysts: A Versatile Approach for Activity Tests and Mechanistic Studies. *Surf. Sci.* **2010**, *604*, 241-244.

98. Rodriguez, J. A.; Ma, S.; Liu, P.; Hrbek, J.; Evans, J.; Perez, M., Activity of Ceox and Tiox Nanoparticles Grown on Au(111) in the Water-Gas Shift Reaction. *Science* **2007**, *318*, 1757-1760.

99. Senanayake, S. D.; Stacchiola, D.; Rodriguez, J. A., Unique Properties of Ceria Nanoparticles Supported on Metals: Novel Inverse Ceria/Copper Catalysts for Co Oxidation and the Water-Gas Shift Reaction. *Acc. Chem. Res.* **2013**, *46*, 1702-1711.

100. Perdew, J. P., Density-Functional Approximation for the Correlation-Energy of the Inhomogeneous Electron-Gas. *Phys. Rev.* **1986**, *33*, 8822-8824.

101. Eichkorn, K.; Weigend, F.; Treutler, O.; Ahlrichs, R., Auxiliary Basis Sets for Main Row Atoms and Transition Metals and Their Use to Approximate Coulomb Potentials. *Theor. Chem. Acc.* **1997**, *97*, 119-124.

102. Weigend, F.; Ahlrichs, R., Balanced Basis Sets of Split Valence, Triple Zeta Valence and Quadruple Zeta Valence Quality for H to Rn: Design and Assessment of Accuracy. *Phys. Chem. Chem. Phys.* **2005**, *7*, 3297-3305.

103. Eichkorn, K.; Treutler, O.; Ohm, H.; Haser, M.; Ahlrichs, R., Auxiliary Basis-Sets to Approximate Coulomb Potentials. *Chem. Phys. Lett.* **1995**, *240*, 283-289.

104. Weigend, F., Accurate Coulomb-Fitting Basis Sets for H to Rn. *Phys. Chem. Chem. Phys.* **2006**, *8*, 1057-1065.

105. Stephens, P. J.; Devlin, F. J.; Chabalowski, C. F.; Frisch, M. J., Ab-Initio Calculation of Vibrational Absorption and Circular-Dichroism Spectra Using Density-Functional Force-Fields. *J. Phys. Chem.* **1994**, *98*, 11623-11627.

106. Austin, N.; Mpourmpakis, G., Understanding the Stability and Electronic and Adsorption Properties of Subnanometer Group Xi Monometallic and Bimetallic Catalysts. *J. Phys. Chem. C* **2014**, *118*, 18521-18528.

107. Graciani, J.; Vidal, A. B.; Rodriguez, J. A.; Sanz, J. F., Unraveling the Nature of the Oxide-Metal Interaction in Ceria-Based Noble Metal Inverse Catalysts. *J. Phys. Chem. C* **2014**, *118*, 26931-26938.

108. Zhu, M.; Lanni, E.; Garg, N.; Bier, M. E.; Jin, R., Kinetically Controlled, High-Yield Synthesis of $Au_{25}$ Clusters. *J. Am. Chem. Soc.* **2008**, *130*, 1138-1139.

109. Taylor, M. G.; Mpourmpakis, G., Thermodynamic Stability of Ligand-Protected Metal Nanoclusters. *Nat. Commun.* **2017**, *8*, 15988.

110. Coperet, C., C-H Bond Activation and Organometallic Intermediates on Isolated Metal Centers on Oxide Surfaces. *Chem. Rev.* **2010**, *110*, 656-680.

111. Banares, M. A., Supported Metal Oxide and Other Catalysts for Ethane Conversion: A Review. *Catal. Today* **1999**, *51*, 319-348.

112. McFarland, E. W.; Metiu, H., Catalysis by Doped Oxides. *Chem. Rev.* **2013**, *113*, 4391-4427.

113. Hargreaves, J. S. J.; Hutchings, G. J.; Joyner, R. W.; Taylor, S. H., A Study of the Methane-Deuterium Exchange Reaction over a Range of Metal Oxides. *Appl. Catal, A.* **2002**, *227*, 191-200.

114. Michorczyk, P.; Ogonowski, J., Dehydrogenation of Propane in the Presence of Carbon Dioxide over Oxide-Based Catalysts. *Reaction Kinetics and Catalysis Letters* **2003**, *78*, 41-47.

115. Nakagawa, K.; Okamura, M.; Ikenaga, N.; Suzuki, T.; Kobayashi, T., Dehydrogenation of Ethane over Gallium Oxide in the Presence of Carbon Dioxide. *Chem. Comm.* **1998**, 1025-1026.

116. Liu, Y.; Li, Z. H.; Lu, J.; Fan, K. N., Periodic Density Functional Theory Study of Propane Dehydrogenation over Perfect Ga2o3(100) Surface. *J. Phys. Chem. C* **2008**, *112*, 20382-20392.

117. Kazansky, V. B.; Subbotina, I. R.; Pronin, A. A.; Schlogl, R.; Jentoft, F. C., Unusual Infrared Spectrum of Ethane Adsorbed by Gallium Oxide. *J. Phys. Chem. B* **2006**, *110*, 7975-7978.

118. Blasco, T.; Nieto, J. M. L., Oxidative Dehydrogenation of Short Chain Alkanes on Supported Vanadium Oxide Catalysts. *Appl. Catal, A.* **1997**, *157*, 117-142.

119. Wachs, I. E.; Weckhuysen, B. M., Structure and Reactivity of Surface Vanadium Oxide Species on Oxide Supports. *Appl. Catal. A.* **1997**, *157*, 67-90.

120. Weckhuysen, B. M.; Schoonheydt, R. A., Alkane Dehydrogenation over Supported Chromium Oxide Catalysts. *Catal. Today* **1999**, *51*, 223-232.

121. Nowak, I.; Ziolek, M., Niobium Compounds: Preparation, Characterization, and Application in Heterogeneous Catalysis. *Chem. Rev.* **1999**, *99*, 3603-3624.

122. Zheng, B.; Hua, W. M.; Yue, Y. H.; Gao, Z., Dehydrogenation of Propane to Propene over Different Polymorphs of Gallium Oxide. *Journ. Catal.* **2005**, *232*, 143-151.

123. Otroshchenko, T.; Sokolov, S.; Stoyanova, M.; Kondratenko, V. A.; Rodemerck, U.; Linke, D.; Kondratenko, E. V., $ZrO_2$-Based Alternatives to Conventional Propane Dehydrogenation Catalysts: Active Sites, Design, and Performance. *Angew. Chem. Int. Ed.* **2015**, *54*, 15880-15883.

124. Lillehaug, S.; Borve, K. J.; Sierka, M.; Sauer, J. A., Catalytic Dehydrogenation of Ethane over Mononuclear Cr(Iii) Surface Sites an Silica. Part I. C-H Activation by Sigma-Bond Metathesis. *J. Phys. Org. Chem.* **2004**, *17*, 990-1006.

125. Lillehaug, S.; Jensen, V. R.; Borve, K. J., Catalytic Clehydrogenation of Ethane over Mononuclear Cr(Iii)-Silica Surface Sites. Part 2: C-H Activation by Oxidative Addition. *J. Phys. Org. Chem.* **2006**, *19*, 25-33.

126. Olsbye, U.; Virnovskaia, A.; Prytz, O.; Tinnemans, S. J.; Weckhuysen, B. M., Mechanistic Insight in the Ethane Dehydrogenation Reaction over $Cr/Al_2O_3$ Catalysts. *Catal. Lett.* **2005**, *103*, 143-148.

127. Labinger, J. A.; Bercaw, J. E., Understanding and Exploiting C-H Bond Activation. *Nature* **2002**, *417*, 507-514.

128. Baerns, M.; Buyevskaya, O., Simple Chemical Processes Based on Low Molecular-Mass Alkanes as Chemical Feedstocks. *Catal. Today* **1998**, *45*, 13-22.

129. Harlin, M. E.; Niemi, V. M.; Krause, A. O. I., Alumina-Supported Vanadium Oxide in the Dehydrogenation of Butanes. *Journ. Catal.* **2000**, *195*, 67-78.

130. Rodemerck, U.; Kondratenko, E. V.; Otroshchenko, T.; Linke, D., Unexpectedly High Activity of Bare Alumina for Non-Oxidative Isobutane Dehydrogenation. *ChemComm* **2016**, *52*, 12222-12225.

131. Valla, M.; Wischert, R.; Comas-Vives, A.; Conley, M. P.; Verel, R.; Coperet, C.; Sautet, P., Role of Tricoordinate Al Sites in $CH_3ReO_3/Al_2O_3$ Olefin Metathesis Catalysts. *J. Am. Chem. Soc.* **2016**, *138*, 6774-6785.

132. Joubert, J.; Delbecq, F.; Thieuleux, C.; Taoufik, M.; Blanc, F.; Coperet, C.; Thivolle-Cazat, J.; Basset, J.-M.; Sautet, P., Synthesis, Characterization, and Catalytic Properties of Gamma-Al2o3-Supported Zirconium Hydrides through a Combined Use of Surface Organometallic Chemistry and Periodic Calculations. *Organometallics* **2007**, *26*, 3329-3335.

133. Joubert, J.; Delbecq, F.; Sautet, P., Alkane Metathesis by a Tungsten Carbyne Complex Grafted on Gamma Alumina: Is There a Direct Chemical Role of the Support? *Journ Catal.* **2007**, *251*, 507-513.

134. Fang, Z. T.; Wang, Y.; Dixon, D. A., Computational Study of Ethanol Conversion on Al8o12 as a Model for Gamma-$Al_2O_3$. *J. Phys. Chem. C* **2015**, *119*, 23413-23421.

135. G. Pacchioni, P. S. B., F. Parmigiani, Cluster Models for Surface and Bulk Phenomena. *NATOASI Series B* **1992**, *283*.

136. Fukui, K., The Path of Chemical-Reactions - the Irc Approach. *Acc. Chem. Res.* **1981**, *14*, 363-368.